ELSEVIER

Contents lists available at ScienceDirect

Science of the Total Environment

journal homepage: www.elsevier.com/locate/scitotenv





The apparent quantum yield matrix (AQY-M) of CDOM photobleaching in estuarine, coastal, and oceanic surface waters

Xiaohui Zhu ^{a,*}, Matthew W. Weiser ^a, Joshua P. Harringmeyer ^a, Karl Kaiser ^b, Brett D. Walker ^c, Simon Bélanger ^d, Chloe H. Anderson ^{e,f}, Cédric G. Fichot ^a

- a Department of Earth and Environment, Boston University, Boston, MA 02215, USA
- b Department of Marine and Coastal Environmental Science, Texas A&M University, Galveston Campus, Galveston, TX, USA
- ^c Department of Earth and Environmental Sciences, University of Ottawa, Ottawa, ON, Canada
- d Department of Biology, Chemistry and Geography, BOREAS, Université du Québec à Rimouski, Rimouski, Québec G5L 3A1, Canada
- e MARUM Center for Marine Environmental Sciences, University of Bremen, Leobener Str. 8, 28359 Bremen, Germany
- f Department of Earth and Planetary Sciences, Harvard University, Cambridge, MA 02138, USA

HIGHLIGHTS

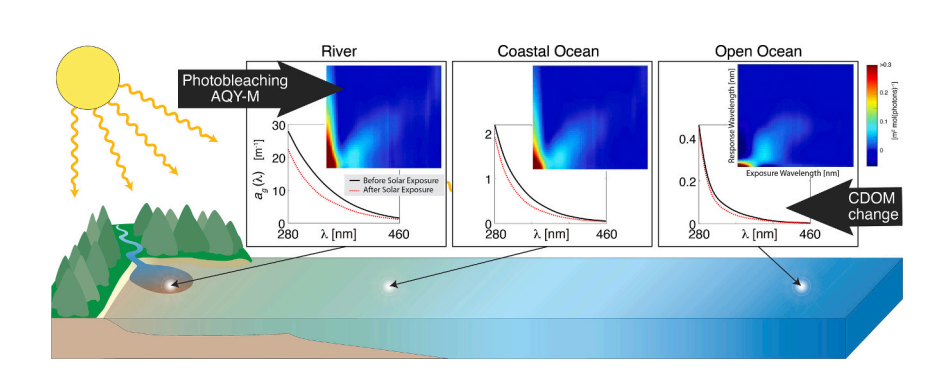
- New method was applied to assess natural variability in CDOM photobleaching AQY-M.
- AQY-M varies with CDOM composition/ origin across land-ocean aquatic continuum.
- AQY-M also depends on water temperature and extent of solar exposure.
- S₂₇₅₋₂₉₅, water temperature, and solar exposure together can predict accurate AQY-M.
- New predictive AQY-M model can help calculate photobleaching rates on large scales.

ARTICLE INFO

Editor: Shuzhen Zhang

Keywords: CDOM Photobleaching AQY Apparent quantum yields

GRAPHICAL ABSTRACT



ABSTRACT

The photochemical degradation of chromophoric dissolved organic matter (CDOM) upon solar exposure, known as photobleaching, can significantly alter the optical properties of the surface ocean. By leading to the breakdown of UV- and visible-radiation-absorbing moieties within dissolved organic matter, photobleaching regulates solar heating, the vertical distribution of photochemical processes, and UV exposure and light availability to the biota in surface waters. Despite its biogeochemical and ecological relevance, this sink of CDOM remains poorly quantified. Efforts to quantify photobleaching globally have long been hampered by the inherent challenge of determining representative apparent quantum yields (AQYs) for this process, and by the resulting lack of understanding of their variability in natural waters. Measuring photobleaching AQY is made challenging by the need to determine AQY matrices (AQY-M) that capture the dual spectral dependency of this process (i.e., magnitude varies with both excitation wavelength and response wavelength). A new experimental approach now greatly facilitates the quantification of AQY-M for natural waters, and can help address this problem. Here, we conducted controlled photochemical experiments and applied this new approach to determine the AQY-M of 27 contrasting water samples collected globally along the land-ocean aquatic continuum (i.e., rivers, estuaries,

^{*} Corresponding author at: Department of Earth and Environment, Boston University, 675 Commonwealth Avenue, Boston, MA 02215, USA. *E-mail address:* zhuxh@bu.edu (X. Zhu).

coastal ocean, and open ocean). The experiments and analyses revealed considerable variability in the magnitude and spectral characteristics of the AQY-M among samples, with strong dependencies on CDOM composition/ origin (as indicated by the CDOM 275–295-nm spectral slope coefficient, $S_{275-295}$), solar exposure duration, and water temperature. The experimental data facilitated the development and validation of a statistical model capable of accurately predicting the AQY-M from three simple predictor variables: 1) $S_{275-295}$, 2) water temperature, and 3) a standardized measure of solar exposure. The model will help constrain the variability of the AQY-M when modeling photobleaching rates on regional and global scales.

1. Introduction

Chromophoric dissolved organic matter (CDOM), the optically active component of dissolved organic matter (DOM), is a major regulator of solar radiation exposure in surface waters ranging from wetlands and rivers to the open ocean. It is also the main precursor for a multitude of ubiquitous photochemical reactions of biogeochemical significance and relevance to climate (Mopper et al., 2015). Its chemical makeup includes a suite of dissolved organic molecules containing conjugated systems, aromatic functional groups, metal complexes, and other components involved in intramolecular charge-transfer (CT) interactions (McKay, 2020; Sharpless and Blough, 2014; Stedmon and Nelson, 2015). These chromophoric moieties contribute to the characteristic shape of the CDOM absorption spectrum, which increases exponentially from the near infrared to the visible and ultraviolet (UV) domains. In the global ocean, CDOM contributes most (>50 %) of the absorption and vertical attenuation of UV/blue solar radiation (Fichot and Miller, 2010; Nelson and Siegel, 2013), meaning it is a major regulator of photosynthetically available radiation (PAR) availability and UV radiation exposure to phytoplankton in surface waters. The variability of CDOM in the surface ocean therefore exerts a direct influence on marine primary productivity and ecosystems functioning (Hickman et al., 2010; Mena et al., 2019).

Exposure to solar radiation in surface waters inevitably leads to the photochemical degradation of DOM chromophoric moieties (Kouassi and Zika, 1992). This process, called photobleaching, results in a net loss of CDOM absorption across the entire spectrum (e.g., 250-700 nm) and has long been considered a significant CDOM degradation pathway in sunlit waters (Del Vecchio and Blough, 2002). This was evidenced by observations of large changes in CDOM absorption during laboratory and deck-based solar-exposure experiments and of major losses in in-situ CDOM absorption in the surface mixed layer during summer (Fichot and Benner, 2012; Helms et al., 2013; Vodacek et al., 1997; Yamashita et al., 2013). Consequently, photobleaching has the potential to significantly affect PAR availability, UV exposure, and solar heating in the surface ocean (Hill, 2008; Swan et al., 2012). Photobleaching also alters the fluorescence properties of dissolved organic matter, imprinting distinctive features in the fluorescence excitation-emission matrix that are frequently used to diagnose past solar exposure (Hansen et al., 2016; Murphy et al., 2018; Tzortziou et al., 2007). Photobleaching also consistently operates faster than the photo-mineralization of dissolved organic carbon (DOC), leading to the decoupling of these two entities' dynamics and complicating the use of CDOM absorption as an optical proxy of DOC concentration (Bonelli et al., 2022; Cao et al., 2018; Del Vecchio and Blough, 2002; Fichot and Benner, 2011).

The rate of photobleaching in sunlit waters and its significance as a sink of CDOM in aquatic systems globally remain poorly quantified (Fichot et al., 2023). The quantification of photobleaching rates on large scales has long been hampered by the challenge of determining representative apparent quantum yields (AQY) for this process (i.e., change in CDOM absorption coefficient per absorbed photon), and by a lack of understanding of their variability in natural waters. A barrier to their determination is the pronounced dual spectral dependency of the photobleaching process –that is, the magnitude of the AQY varies with both the wavelength of exposure and the response wavelength (Del Vecchio and Blough, 2002; Zhu et al., 2020). This implies the AQY should be represented by a spectral matrix rather than a single spectrum. Studies

have developed models of photobleaching efficiency that account for this dual dependency (Goldstone et al., 2004; Osburn et al., 2001; Swan et al., 2012; Tzortziou et al., 2007), but these efforts have been very limited in scope and applicability. A new approach was recently developed to facilitate the determination of accurate and reproducible photobleaching AQY matrices (AQY-M) for natural water samples (Zhu et al., 2020). The study also revealed a strong dependency of the AQY-M on the degradation state of CDOM, water temperature, and solar-exposure duration. However, this study was also limited in scope and the natural variability of the photobleaching AQY-M across the land-ocean aquatic continuum remains unknown. The quantitative understanding of photobleaching will be limited for as long as the variability of the AQY-M remains uncharacterized and unconstrained.

Here, we applied this new methodology to 27 surface water samples spanning the land-ocean aquatic continuum, in order to 1) evaluate the natural variability of the photobleaching AOY-M, and 2) develop a predictive model of AQY-M applicable across most water types. A selected subset of samples was exposed to controlled simulated sunlight at different water temperatures and for different durations (e.g., 24 and 48 h), thereby providing a total of 71 distinct, measured AQY-M to assess variability and sensitivity to temperature and exposure duration, and to support the model development and validation. The development of a predictive model involved a principal component analysis of the measured AQY-M data set and the production and comparison of various approaches to predict principal component scores from three variables: 1) the 275–295-nm spectral slope coefficient of CDOM, $S_{275-295}$, as an indicator of CDOM composition, 2) a standardized measure of solar exposure, and 3) water temperature. An independent data set generated using single-cutoff solar exposures of independent samples provided an additional independent validation data set to confirm model performance in a completely independent environment not included in the model development.

2. Data and Methods

2.1. Field data and water sample collection, processing, and preservation

A total of 27 distinct water samples were collected for use in experiments aimed to determine AQY-M. Samples were collected in surface waters along the freshwater-marine continuum, across a large latitudinal gradient (64.50°S to 49.20°N), and in the major ocean basins. The samples were collected in various, contrasting aquatic environments spanning rivers, estuaries, salt marshes, river-influenced coastal waters, coastal upwellings, and the open ocean (Fig. 1A-C and Supplementary Tables S1–S2). An additional set of 12 samples used strictly for an extra, independent validation of the model was collected in the nearshore coastal waters of Louisiana in Spring 2021 (n = 7) and Fall 2021 (n = 5) (Fig. 1D and Supplementary Table S3). Salinity at the sampling sites was measured using either a calibrated Yellow Springs Instruments (YSI) ProDSS sonde equipped with a temperature-conductivity sensor (e.g., when sampling from small boats), or a SeaBird Temperature-Conductivity-Depth instrument mounted on a rosette (e.g., when sampling from oceanographic vessels). Two different protocols were used to filter and preserve the samples depending on their provenance:

Freshwater and estuarine water samples — Samples from rivers, estuaries and salt marshes (typically salinity $<\!32$) were obtained with small boats and collected near the surface ($<\!1$ m) using a 4-L horizontal Van Dorn sampler rinsed at least three times with ambient water. Samples were then filtered within a few hours of collection through a pre-combusted 0.7-µm glass-fiber filters (GF/F furnaced at 450 °C for 6 h) or a 0.8-µm nylon-membrane filter cartridge (acid washed with 1 % hydrochloric acid and rinsed with Milli-Q water). The filtrate was collected in clean (acid washed; furnaced at 450 °C for 6 h) borosilicate glass bottles with Teflon-lined closures and kept in the dark and at 4 °C for up to 48 h. Samples were then filtered again through clean 0.2-µm nylon membrane filters (47-mm-diameter, Whatman) immediately before experiment.

Ocean water samples — Samples from oceanic waters including some coastal waters (typically salinity $>\!32$) were obtained from ships and collected near the surface ($<\!5$ m) using a Conductivity-Temperature-Depth (CTD) rosette equipped with Niskin bottles. Samples were immediately gravity-filtered from the Niskin bottles using precombusted 0.7-µm glass-fiber filters (GF/F furnaced at 540 $^{\circ}\text{C}$ for

2 h; Druffel et al., 2021), and collected in clean (acid washed, furnaced at 450 °C for 6 h) borosilicate glass bottles with Teflon-lined closures. Samples were then immediately frozen (-20 °C) until the experiments. Samples were then filtered again through clean 0.2- μ m nylon membrane filters (47-mm-diameter, Whatman) immediately before experiment. The majority the ocean water samples used in this study were collected from the GO-SHIP cruises P18 in 2016/2017 and IO7N in 2018 onboard the R/V Ronald H. Brown, and from cruise MR157 onboard the R/V Meteor in 2019.

2.2. Methodology overview

A flowchart summarizing the methodology used in this study is presented in Fig. 2. Briefly, the 27 water samples were used in controlled photochemical experiments using the same experimental design and setup as in Zhu et al. (2020). The measurements resulting from these experiments were then used to generate *measured AQY-M* using the approach presented in Zhu et al. (2020), and to calculate simple predictor variables to estimate AQY-M. The resulting database of *measured*

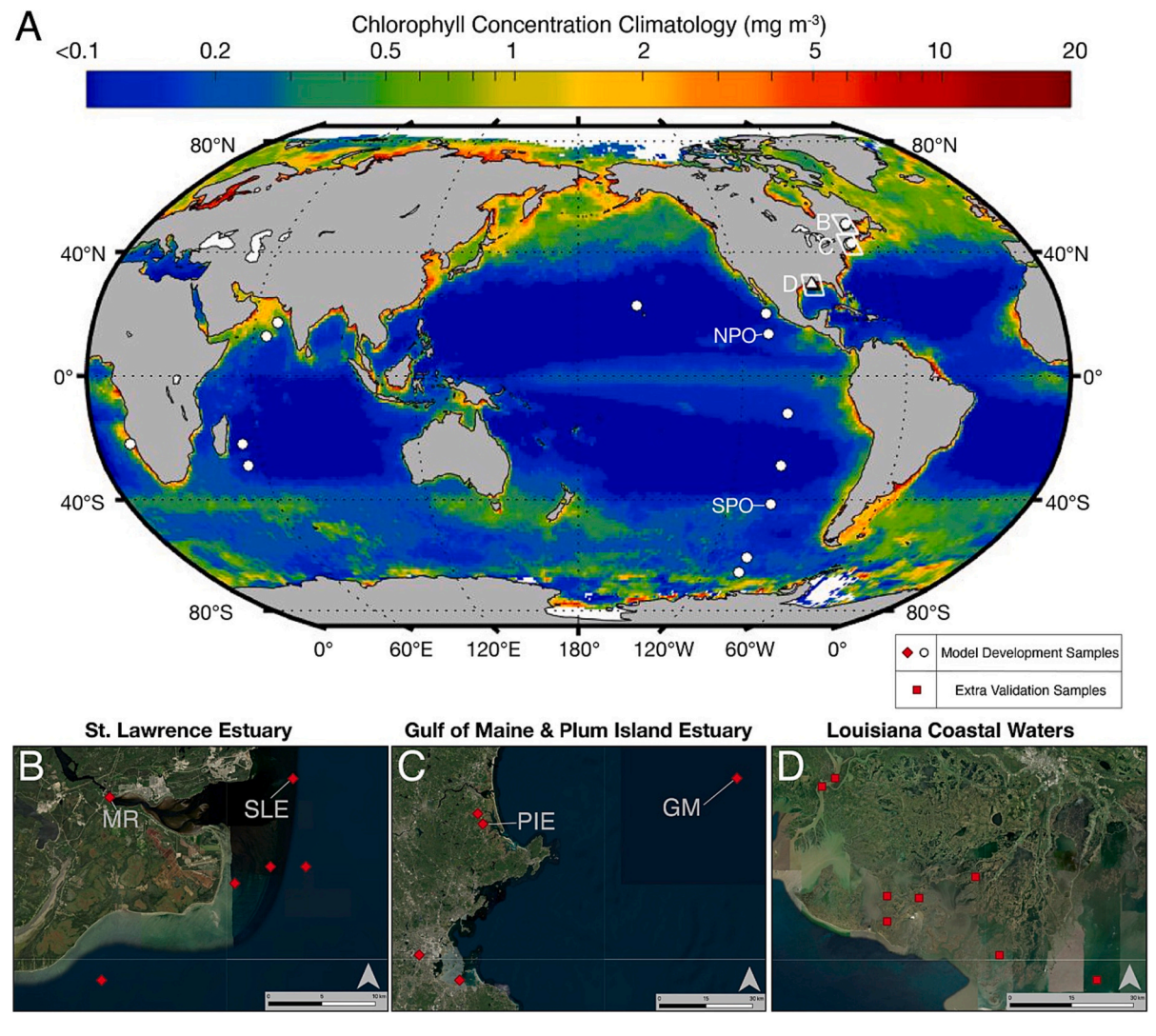


Fig. 1. Locations of water samples collected and used in photochemical experiments for this study. Water samples were collected worldwide in a wide range of aquatic environments along the land-ocean continuum including riverine, estuarine, coastal, and open-ocean waters. Named locations on the map point to samples presented in figures shown later in the manuscript: NPO (North Pacific Ocean), SPO (South Pacific Ocean), MR (Manicouagan River), SLE (St. Lawrence Estuary), PIE (Plum Island Estuary), and GM (Gulf of Maine). (A) Sample locations superimposed on a global climatology (2002–2020) of surface chlorophyll-a concentration estimated from ocean-color remote sensing, showing the samples originated from waters with very different levels of biomass. (B) Close-up view of the St-Lawrence Estuary (Manicouagan River, near Baie-Comeau, Québec) with sampling locations. (C) Close-up view of the Gulf of Maine and Plum Island Estuary with sampling locations. (D) Close-up view of Louisiana Coastal Waters (Atchafalaya River and Terrebonne Bay) with locations of samples used for the extra validation.

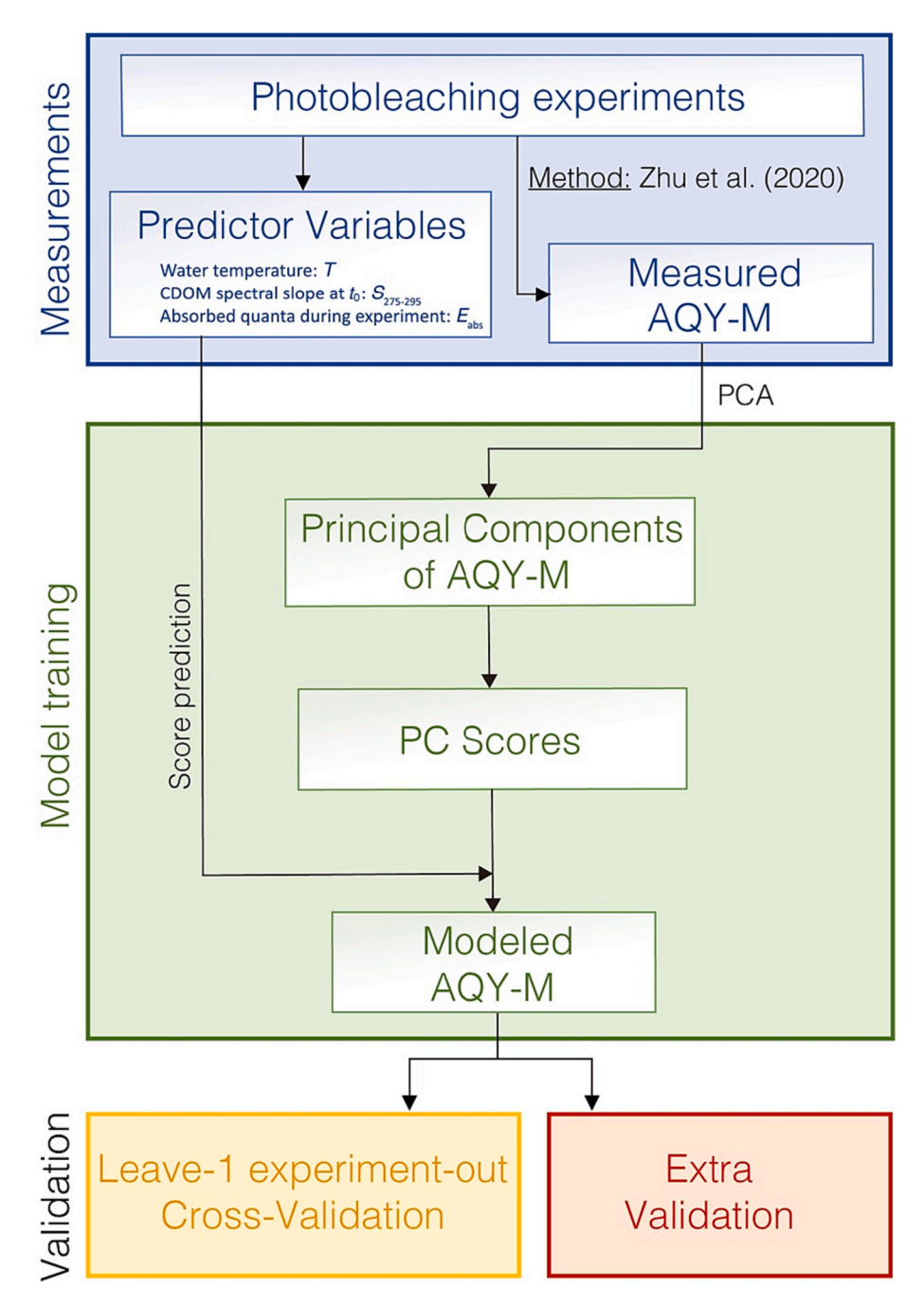


Fig. 2. Flowchart summarizing the methodology used to develop and validate the predictive model of AQY-M. The measurements derived from the photochemical experiments were used with the method of Zhu et al. (2020) to produce a set of measured AQY-M representative of different water samples, temperature treatments, and exposure durations. This database of measured AQY-M was then used in a principal component analysis (PCA) to calculate the AQY-M principal components (PC) and their corresponding scores. A model was then trained to predict the PC scores from three predictor variables (e.g., water temperature, $S_{275-295}$, and a standardized measure of solar exposure) on which the AQY-M were observed to have a dependency. The predicted PC scores were then used in linear combinations of the PCs to predict the modeled AQY-M. A leave-1 experiment-out cross-validation and an extra independent validation were then used to quantify the uncertainties associated with the predicted $a_g(\lambda)$.

AQY-M was then used as input to a principal component analysis that retained the first three principal components (matrices). A model to predict the scores of these principal components from the predictor variables and to construct *modeled AQY-M* was then developed, and the model's ability to reproduce reasonably accurate versions of the *measured AQY-M* was assessed. Finally, the model's ability to reproduce measured changes in spectral CDOM absorption coefficient during the experiments was assessed two different ways: 1) using a leave-1 experiment-out cross-validation with all data used in the model development, and 2) by implementing the model on the extra validation data set

collected in coastal Louisiana. This extra set of samples from Louisiana was obtained opportunistically via participation into another project, and was used specifically to assess the performance of the model when applied to a completely new environment not considered in the model development—in this case, a sub-tropical coastal environment.

2.3. CDOM photobleaching experiments: design and setup

All filtered water samples were irradiated under controlled and monitored illumination conditions using an Atlas Suntest XLS+ solar

simulator (Xenon lamp) equipped with a custom-made, temperaturecontrolled sample exposure system. The experimental setup and general methodology are described in detail in Zhu et al. (2020). Briefly, all irradiations were done at maximum lamp output (765 W m⁻²) but without the "daylight" glass filter normally used to filter out UV-C and most UV-B radiation. Instead, solar exposure of the sample was controlled using Schott optical long-pass filters (cut-off wavelengths λ_c = 280, 295, 305, 320, 345, 385, 420, and 475 nm), enabling up to eight different spectral treatments simultaneously. For each spectral treatment, the sample was irradiated end-on in a tightly sealed (solid polypropylene caps, Teflon-lined silicon septa), 2.5-cm diameter spectrophotometric quartz cell (Spectrocell Inc.) with a 5-cm pathlength oriented vertically just below the cutoff filter. The cells were immersed in water kept at constant temperature by a circulating water bath, and kept in fixed position using a custom-made, black-anodized aluminum frame that minimized horizontal exchange of solar radiation between cells. Details about the experiments are provided in Supplementary Table S4, and two different major types of photochemical experiments were conducted:

Experiments to produce measured AQY-M — The experiments used to

calculate the measured AQY-M all involved eight simultaneous spectral cut-off treatments (cut-off wavelengths $\lambda_c = 280, 295, 305,$ 320, 345, 385, 420, and 475 nm). In this case, experiments for all samples (n = 27) were at least conducted at a temperature of 20 °C and included at least a 48-h exposure with spectrophotometric measurements of CDOM absorption (see method description below) made at the initial time ($t_0 = 0$ h) and at the final time ($t_{48} = 48$ h). For a subset of samples (n = 8), the experiment was repeated at two additional water temperatures (5 °C and 35 °C) to help assess temperature dependence of the AQY-M. For a subset of samples (n = 14), which includes the 8 samples treated at different temperatures, the experiment also included intermediary spectrophotometric measurements of CDOM absorption after 24-h exposure time, thereby providing measurements collected at $t_0 = 0$ h, $t_{24} = 24$ h, and $t_{48} = 0$ 48 h. This combination of contrasting samples and different treatments facilitated the calculation of 71 distinct AQY-M and provided sufficient solar exposure conditions to assess dependencies and to constrain the predictive models. To facilitate model development, interpolation of the measurements to every hour between 0 and 48 h exposure time generated an expanded data set of 2064 AQY-M. Experiments for extra independent validation of the AQY-M model – The experiments used for the extra independent validation of the model involved exposing eight replicates of each sample (n = 12) with the same 320-nm cutoff spectral treatment. The 320-nm cutoff filter (meaning a ~50 % transmission at 320 nm) produced a solar exposure in the solar simulator that was the most spectrally representative of that typically experienced in natural waters (Zhu et al., 2020), making this experimental design desirable for validation. The experiments were conducted at a water temperature of 20 °C, although two of the 12 samples were also exposed at 5 °C and at 35 °C. The experiments involved CDOM spectrophotometric measurements made either at $t_0=0$ h and $t_{24}=24$ h, or at $t_0=0$ h and $t_{48}=48$ h. For each experiment, note that the 8 replicates of the same sample were exposed to slightly different exposures ($\sim\pm10$ %) due to the spatially uneven exposure within the solar simulator. However, these differences in exposure were monitored and adequately accounted for in the validations. Overall, these experiments produced a total of 148 observations for the extra, independent validation (Zhu et al., 2020). This set of simpler and less tedious experiments aimed specifically at assessing the performance of the model when applied to a completely independent environment.

2.4. Spectrophotometric measurements of CDOM, and calculation of related variables

Spectrophotometric methods — Two different methods were used to make spectrophotometric measurements of CDOM absorption coefficient spectra (range used here 275 nm to 700 nm) depending on sample provenance. For both methodology, measurements were made against a blank of purified water (Millipore Milli-Q water) after samples and blanks were equilibrated to room temperature (Pegau et al., 1997). For freshwater and estuarine water samples, the CDOM absorption spectra of freshwater and estuarine samples were measured using a Perkin Elmer Lambda-650 UV-visible dual-beam spectrophotometer and 5-cm pathlength cylindrical quartz cells (Fichot and Benner, 2011; Zhu et al., 2020). For ocean water samples, the CDOM absorption spectra of ocean samples were measured using a TiDAS S300 UV/VIS (190-720-nm, 1-nm resolution) photodiode array (PDA) spectrophotometer system equipped with an integrated deuterium light source, and outfitted with a 100-cm liquid waveguide capillary cell (LWCC, Word Precision Instrument), following recommended protocols (Mannino et al., 2019). Additional details about these established methods are provided in Supplementary Text S1.

Temporal interpolation of CDOM absorption coefficient during exposure — For each experiment, the absorption coefficient spectra, $a_{\rm g}(\lambda,t)$, measured at the t_0 , t_{24} and/or t_{48} time points were interpolated to hourly values using a cubic Hermite interpolation method, which uses a continuous first derivative that provides realistic, smooth, non-linear interpolations. Three interpolations with different endmember assumptions were used, and the average value was used as the final interpolated absorption coefficient. A representative set of interpolation examples are presented in Supplementary Fig. S1, and additional details are provided in Supplementary Text S2.

Change in CDOM absorption coefficient — The difference in CDOM absorption coefficients spectra between the initial time point, t_0 , and any other time point, t during the photobleaching experiments, is denoted here as $\Delta a_{\rm g}(\lambda_{\rm re},t)$ and was calculated as in Eq. (1):

$$\Delta a_{g}(\lambda_{re}, t) = a_{g}(\lambda_{re}, t) - a_{g}(\lambda_{re}, t_{0}) \tag{1}$$

CDOM absorption spectral slope coefficients — The spectral dependence of the CDOM absorption coefficient can be described accurately over narrow spectral ranges using an exponential function of the form shown in Eq. (2):

$$a_g(\lambda) = a_g(\lambda_0)e^{-S(\lambda - \lambda_0)} \tag{2}$$

where λ_0 is a reference wavelength, and S is the spectral slope coefficient over the narrow spectral range, λ_0 - λ -nm. Here, the spectral slope coefficient over the 275–295 nm spectral range, $S_{275-295}$, was calculated using a linear regression of $\ln(a_{\rm g}(\lambda))$ on λ from 275 to 295 nm. Similarly, the spectral slope coefficient for the 350–400 nm spectral range, $S_{350-400}$, was calculated using a linear regression of $\ln(a_{\rm g}(\lambda))$ on λ from 350 to 400 nm.

2.5. Calculation of quanta absorbed by CDOM during solar exposure

The spectrum of quanta (photons) absorbed by CDOM during irradiation, denoted here as $\overline{E_{abs}}(\lambda_{ex},t)$, is a key variable used in the determination of the AQY-M (Zhu et al., 2020). The method to calculate $\overline{E_{abs}}(\lambda_{ex},t)$ is described in detail in Fichot and Benner (2014) and was further described and successfully applied and validated using nitrite actinometry in Zhu et al. (2020). Briefly, $\overline{E_{abs}}(\lambda_{ex},t)$ was calculated for each spectral treatment and exposure time interval using $a_g(\lambda_{re},t)$ and measurements of incident irradiance made with a high-performance

UV–visible scanning OL-756 spectroradiometer equipped with a 2-inches integrating sphere (OL-IS-270) and calibrated against a NIST-traceable standard of spectral irradiance (OL-752-10E) operated with a high-precision DC-current lamp source (OL-410-200). Details about the calculations are provided in Supplementary Text S3.

2.6. Calculation of AQY-M from experiments (measured AQY-M)

The methodology used to determine the CDOM photobleaching AQY-M for all the samples —the *measured AQY-M* — is described in detail in Zhu et al. (2020). Briefly, the methodology involves two sequential steps. First, a partial least square regression of the measured $\Delta a_g(\lambda_{re},t)$ on the measured $\overline{E_{abs}}(\lambda_{ex},t)$ was done to derive coefficients and intercepts facilitating the reproduction of the observed $\Delta a_g(\lambda_{re},t)$ from the observed $\overline{E_{abs}}(\lambda_{ex},t)$ using a matrix operation (\times), where $\textbf{\textit{B}}$ is a matrix of regression coefficients and $B_0(\lambda_{re})$ is a vector of intercept values as shown in Eq. (3):

$$\Delta a_{g}(\lambda_{re}, t) = \overline{E_{abs}}(\lambda_{ex}, t) \times \mathbf{B} + B_{0}(\lambda_{re})$$
(3)

Second, gradient-descent optimization of the coefficient matrix \boldsymbol{B} was done to produce an optimized matrix \boldsymbol{B}' able to generate $\Delta a_g(\lambda_{re},t)$ from $\overline{E_{abs}}(\lambda_{ex},t)$ with similar accuracy as in Eq. (3), but without the use of the intercept values $B_0(\lambda_{re})$, as shown below in Eq. (4):

$$\Delta a_{g}(\lambda_{re}, T) = \overline{E_{abs}}(\lambda_{ex}, T) \times \mathbf{B}'$$
(4)

Here, the optimized B matrix corresponds to an actual AQY-M denoted here as $\Phi_{PB}(\lambda_{ex}, \lambda_{re})$, the AQY-M. Additional details about the approach are provided in Supplementary Text S4 and in Zhu et al. (2020).

2.7. Predictions of AQY-M from simple variables (modeled AQY-M)

The development of a model to predict *modeled AQY-M* from three simple predictor variables ($S_{275-295}$, water temperature, and a standardized measure of solar exposure) involved two steps: (1) a principal component analysis (PCA) used to reduce the dimensionality of the *measured AQY-M* data set by determining principal components (PC) and corresponding PC scores, and (2) a model to predict those PC scores from the three simple predictor variables.

Dimensionality reduction of the AQY-M: It is practical to reduce the dimensionality of the measured AQY-M to develop predictive models of AQY-M from a few simple predictor variables. The measured AQY-M are spectrally complex but include extensive multi-collinearity (Zhu et al., 2020). The observed variance can therefore be summarized by a few rotated versions of the original variables. Here, a PCA was used to reduce the dimensionality of the measured AQY-M and help constrain their observed variability, and was implemented using MATLAB® (2022a version, pca function). The measured AQY-M was thus expressed as in Eq. (5):

$$\Phi_{PB}(\lambda_{ex}, \lambda_{re}) = s_1 P_1 + s_2 P_2 + \dots + s_n P_n$$
(5)

where $P_1, P_2, ..., P_n$ are the PC determined by the PCA, and $s_1, s_2,, s_n$ are the corresponding scores. $P_1, P_2, ..., P_n$ have the same dimensions (201 \times 421) as $\Phi_{\rm PB}(\lambda_{\rm ex}, \lambda_{\rm re})$ and the scores $s_1, s_2,, s_n$ are scalar values. Here, the number of components n=2064.

PC-score prediction model: A model was developed to predict the measured PC scores (s_1, s_2, \ldots, s_n) and facilitate the estimation of *modeled AQY-M* from three predictor variables: 1) a standardized measure of solar exposure of CDOM, 2) the CDOM spectral slope coefficient $S_{275-295}$ used here as compositional indicator of CDOM and 3) water temperature. The proposed AQY-M prediction model includes three sequential steps:

Step 1–Determining the standardized solar exposure of CDOM: The first step consists in determining the solar exposure experienced by CDOM over a duration of interest (e.g., 12 h, 24 h). As observed in Zhu et al. (2020) and in this study, the *measured AQY-M* exhibits a complex dependency on solar exposure. It is therefore important to generate *modeled AQY-M* that are representative of the solar exposure experienced by CDOM in natural waters over a duration of interest. However, because exposure time in the solar simulator is not directly comparable to the exposure time in natural waters, it is critical to develop a measure of solar exposure that is compatible with both contexts. To address this issue, we defined the quantity t_{std} that we referred here to as "standardized solar exposure" and calculated as in Eq. (6):

$$t_{std} = \frac{\overline{E_{abs}}(290 - 350)}{a_g(350)^{0.92}} \tag{6}$$

where $\overline{E_{abs}}(290-350)$ is the amount of quanta from 290-to-350 nm absorbed by CDOM on average in the volume of interest (e.g., cell or mixed layer depth) for a specific exposure duration, and $a_o(350)$ is the absorption coefficient of CDOM at 350 nm. In the solar simulator experiments, $\overline{\textit{E}_{abs}}(290-350)$ varies, to a first order, as a function of the CDOM absorption coefficient. This is largely because the pathlength of solar radiation through the sample cells is very short (5 cm). As a result, $\overline{E_{abs}}(290-350)$ varied dramatically among the samples for the same irradiation duration (Supplementary Fig. S2A). However, this is not the case in the mixed layer (typically >10 m deep), where most of the incident photons in the 290-350 nm range are absorbed by CDOM and $\overline{E_{abs}}(290-350)$ is much less dependent on the CDOM absorption coefficient. In order to minimize this artifact of the experiments and generate a more standardized value of solar exposure (Supplementary Fig. S2B), the calculated $\overline{E_{abs}}(290-350)$ was normalized by $a_g(350)$. Remaining discrepancies among samples were largely removed using an empirically-determined exponent value of 0.92 (Supplementary Fig. S2C and Text S5) applied to $a_g(350)$, as shown in Eq. (6). The resulting t_{std} represented a measure of absorbed quanta by CDOM that scaled more uniformly with exposure duration across the different samples (Supplementary Fig. S2C), thereby facilitating the scaling to solar exposure experienced by CDOM in natural waters. To facilitate the implementation of Step 2 in the model, the t_{std} for each experiment was divided into 48 regular increments (Supplementary Text S5) to match the 48-h duration and the 48 time-interpolated AQY-M determined for each experiment.

Step 2–Predicting the PC scores from $S_{275,295}$: The second step directly predicts the PC scores of the AQY-M from the measured $S_{275-295}$ of the original sample, used here as an indicator of CDOM composition/degradation state. Specifically, for each of the 48 increments in t_{std} , the scores were predicted as in Eq. (7):

$$\widehat{s}_i(20^{\circ}C, t_{std}) = k_i(t_{std}) * S_{275-295} + l_i(t_{std})$$
(7)

where $\widehat{s}_i(20^{\circ}\mathrm{C},t_{std})$ is the predicted score for the i^{th} PC of the AQY-M at 20 °C and for a given t_{std} , and $k_i(t_{std})$ and $l_i(t_{std})$ are coefficients (slope and intercept, respectively) derived from the linear regression of the measured scores $s_i(20^{\circ}\mathrm{C},t_{std})$ on the $S_{275-295}$ measured at the initial time point (i.e., prior to irradiation). A relationship of this form was parameterized for each increment of t_{std} .

Step 3—Temperature adjustment of predicted PC scores: The third and final step aims to adjust the scores predicted in Step 2 for the effects of water temperature using an Arrhenius-type function, as shown in Eq. (8):

$$\widehat{s}_{i}(T, t_{std}) = \widehat{s}_{i}(20^{\circ}\text{C}, t_{std}) * e^{b_{i} \left((T-20) / 293.15^{*}(T+273.15) \right)}$$
(8)

where, $\hat{s}_i(T, t_{std})$ is the PC score for the i^{th} component for a water temperature T, and b_i is a coefficient equal to 1422 and determined empirically from fitting the data from the eight experiments conducted at different water temperatures with Eq. (8).

Calculating the modeled AQY-M: The modeled AQY-M for any particular combination of t_{std} , $S_{275-295}$, and T values was generated with a linear combination of the scores \hat{s}_i predicted by the model with the PC matrices derived from PCA, as shown in Eq. (9):

$$\widehat{\Phi}_{PB}(\lambda_{ex}, \lambda_{re}) = \widehat{s}_1 P_1 + \widehat{s}_2 P_2 + \widehat{s}_3 P_3 \tag{9}$$

where $\widehat{\Phi}_{PB}(\lambda_{ex},\lambda_{re})$ is the predicted AQY-M and $\widehat{s}_1,\widehat{s}_2,\widehat{s}_3$ are the scores of the first 3 PC (Supplementary Text S6) predicted by the PC-score prediction model.

2.8. Model validation

Two approaches were used to validate the model and evaluate its performance using independent data sets: 1) a leave-1 experiment-out method, and 2) a simple implementation on an extra data set (the extra independent validation).

- 1. In the leave-1 experiment-out validation, the AQY-M model was generated using the *measured AQY-M* from 42 of the 43 experiments and was validated using the *measured AQY-M* of the $43^{\rm rd}$ "left-out" experiment. This validation simulated the development of the model and its application on an independent $43^{\rm rd}$ water sample, as the *measured AQY-M* from the "left-out" experiment were not used to train the model. This process was iterated 43 times, using a different "left-out" experiment each time, and the *modeled AQY-M* and modeled $a_g(\lambda)$ spectra after 48-h exposure were compared to their measured equivalents to assess performance and quantify uncertainties associated with the modeled quantities (Supplementary Table S5).
- 2. An extra validation with independent samples collected in the nearshore coastal waters of Louisiana (Fig. 1D) applied the final model on the data from the 15 extra photobleaching experiments (Supplementary Tables S3–S4). These experiments only included 320-nm cut-off treatments, so no *measured AQY-M* were available and only the modeled $a_{\rm g}(\lambda)$ spectra after 48-h exposure were compared to their measured equivalents. However, multiple replicates were available for each experiments, thereby providing a total of 148 $a_{\rm g}(\lambda)$ spectra for comparison. As mentioned earlier, this extra validation specifically aimed to assess the performance of the model

when applied to a completely new environment not used in the model development.

3. Results

3.1. Diversity of CDOM properties and salinity for samples used in this study

The 27 samples used in the AQY-M experiments were broadly representative of surface water types typically encountered between rivers and the open ocean (Fig. 3). The samples originated from multiple rivers, estuaries, marsh-influenced coastal waters, river-influenced ocean margins, coastal upwelling zones, and various open-ocean regions with contrasting nutrient regimes and productivity levels. The salinity of the samples ranged from 0.1 to about 36.2, and their CDOM absorption coefficient at 350 nm, $a_o(350)$, ranged 1000-fold from 0.027 to 24.73 m⁻¹, with corresponding $S_{275-295}$ values ranging from 0.013 to $0.058~\mathrm{nm}^{-1}.$ The $a_{\mathrm{g}}(350)$ decreased more or less linearly with increasing salinity (Fig. 3A), and decreased exponentially and mostly monotonically with increasing $S_{275-295}$ (Fig. 3B). As a result, $S_{275-295}$ increased exponentially with increasing salinity (Fig. 3C). Most of the samples (n = 21/27) were from waters with salinities >25, and more than half of them were from waters with salinities >32. The samples were distributed mostly evenly along the gradients of salinity and CDOM absorption properties (e.g., $a_g(350)$, $S_{275-295}$). Overall, these samples represented a diverse and balanced set for evaluating the natural variability of the photobleaching AQY-M and for developing a model applicable to aquatic systems encountered along the land-ocean continuum.

3.2. Effects of solar exposure on CDOM absorption spectra

Solar exposure in the 320-nm cutoff treatment led consistently to a decrease in the $a_g(\lambda)$ spectrum and to an increase in $S_{275-295}$ in all samples (Fig. 4). After 48 h of exposure at 20 °C in this treatment, $a_g(350)$ decreased on average by 36.5 %, and $S_{275-295}$ increased on average by 22.3 % (Fig. 4A–C). In contrast, the effects of solar exposure on $S_{350-400}$ were less predictable, with both negative and positive changes being observed (Fig. 4C) and an average change of -7.3 %. The 320-nm cutoff treatment was used for this assessment, as it was the most spectrally representative of solar exposure in natural waters (Zhu et al., 2020). Solar exposure also led to a decrease in $a_g(\lambda)$ in the other cut-off treatments, although the magnitude and spectral characteristics of the $a_g(\lambda)$ loss varied strongly depending on the cut-off treatment considered (Supplementary Figs. S3–S5). Specifically, the $a_g(\lambda)$ loss was always

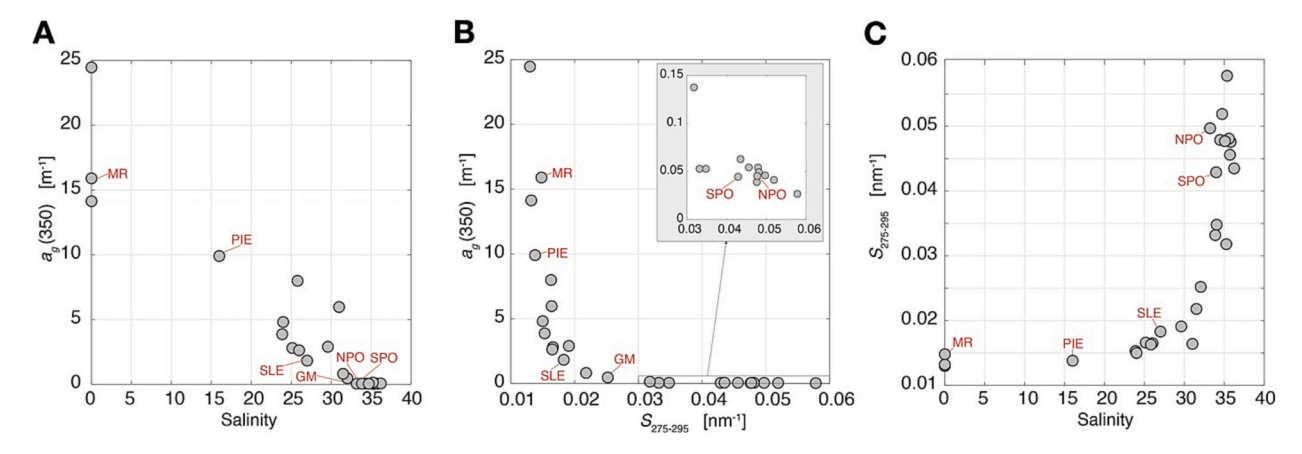


Fig. 3. Relationships between salinity, $a_g(350)$ (CDOM absorption coefficient at 350 nm), and $S_{275-295}$ (CDOM spectral slope coefficient in the 275–295-nm range) for the samples used in the experiments (n=27). The range of these parameters highlight the diversity of samples collected for this study (salinity range: 0.1–36.22; $a_g(350)$ range: 0.027–24.73 m⁻¹; $S_{275-295}$ range: 0.013–0.058 nm⁻¹). (A) Relationship between salinity and $a_g(350)$. (B) Relationship between $S_{275-295}$ and $a_g(350)$. The inset panel shows the data with $S_{275-295}$ ranging from 0.03 to 0.06 nm⁻¹. (C) Relationship between salinity and $S_{275-295}$.

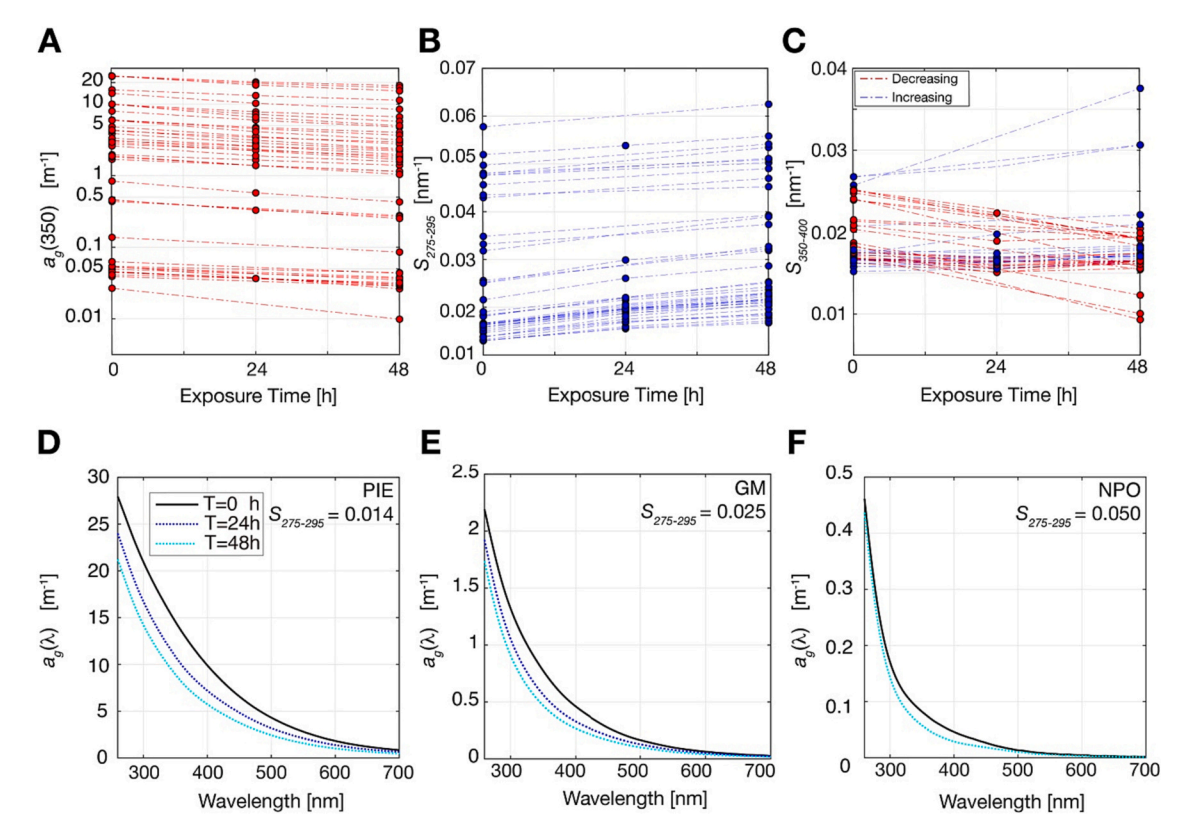


Fig. 4. Effects of photobleaching on the CDOM absorption coefficient spectra and on the spectral slope coefficients during exposure in the solar simulator shown here for the 320-nm cutoff filter treatment. (A, B, C) Change in $a_g(350)$, $S_{275-295}$, and $S_{350-400}$ observed during exposure in the 320-nm cutoff treatment for all 43 different treatments (27 different samples treated at 20 °C, with 8 of these samples being subject to two additional temperature treatments at 5 °C and 35 °C). Solid points correspond to measurements, and dash lines help visualize the direction of change. Black circles/lines indicate an increase during exposure whereas red circles/lines indicate a decrease during exposure (observed for $S_{350-400}$ and $a_g(350)$). (D, E, F) $a_g(\lambda)$ spectra before and after 24-h and 48-h exposures in the solar simulator (20 °C water temperature, and 320-nm cutoff filter) shown here for three contrasting water samples: estuarine water (PIE, after 24 and 48 h exposure), coastal ocean (GM, after 24 and 48 h exposure), and open ocean (NPO, after 48 h exposure only).

largest in the 280-nm cutoff treatment and progressively decreased with increasing cut-off wavelength. Minimal loss in $a_g(\lambda)$ was always observed in the 475-nm cut-off treatment, indicating that solar radiation >475 nm contributed negligibly to photobleaching.

The experiments also revealed significant variability in both the magnitude and spectral characteristics of $a_g(\lambda)$ loss among the samples

(Fig. 4). For the same exposure conditions (48 h of exposure, 20 °C water temperature, 320-nm cut-off treatment), the relative loss of a_g (350) ranged three-fold (19 % - 63 % with a median of 37.3 %) depending on the sample, whereas the increase in $S_{275-295}$ ranged ten-fold (4 %–42 % with a median of 24.2 %) and the change in $S_{350-400}$ ranged from -49 % to 46 % with a median of -1.3 %. The spectral dependency of the

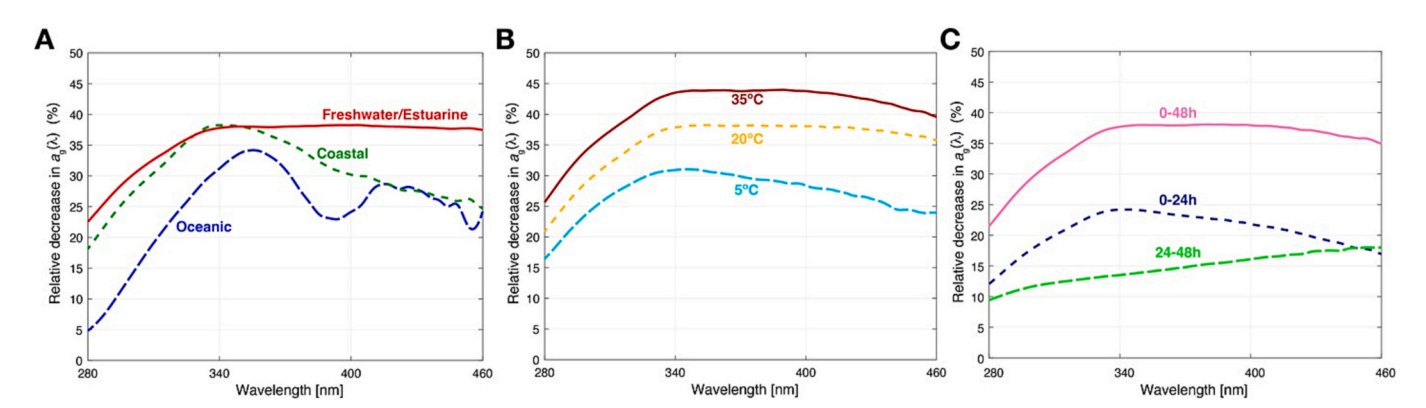


Fig. 5. Average relative decrease in $a_g(\lambda)$ spectra caused by photobleaching (% $a_g(\lambda)$ loss) between contrasting freshwater/estuarine, coastal, and oceanic samples, and for different water temperatures. (A) Relative decrease in $a_g(\lambda)$ spectra for all 27 samples exposed under the same conditions (48-h exposure, 20 °C, 320-nm cutoff filter), and averaged for three categories of samples defined using $S_{275-295}$ thresholds to generate groups with a similar number of observations: Freshwater/Estuarine ($S_{275-295} < 0.0165 \text{ nm}^{-1}$, n = 8), Coastal ($0.0165 \text{ nm}^{-1} < S_{275-295} < 0.040 \text{ nm}^{-1}$, n = 9), Oceanic ($S_{275-295} > 0.040 \text{ nm}^{-1}$, n = 10). The average $S_{275-295}$ and salinity for the three categories are: Freshwater/Estuarine ($S_{275-295} = 0.0145 \text{ nm}^{-1}$, Salinity = 12.81), Coastal ($S_{275-295} = 0.0234 \text{ nm}^{-1}$, Salinity = 30.54), and Oceanic ($S_{275-295} = 0.0483 \text{ nm}^{-1}$, Salinity = 35.01). (B) Relative decrease in $a_g(\lambda)$ spectra corresponding to the 8 samples exposed at multiple water temperatures (5, 20, and 35 °C) after 48-h exposure in the 320-nm cutoff treatments. (C) Relative decrease in $a_g(\lambda)$ spectra observed between 0 and 24 h of exposure, 24–48 h of exposure, and 0–48 h exposure in the 320-nm cutoff treatments of 14 samples.

relative change in $a_{\rm g}(\lambda)$ was also variable among samples. This difference was evident when comparing the $a_{\rm g}(\lambda)$ loss after 48 h of exposure of the PIE, GM, and NPO samples, which correspond to estuarine, coastal, and open-ocean waters in this data set, respectively (Fig. 4D–F). The relative loss of $a_{\rm g}(\lambda)$ appeared relatively homogeneous across the entire UV–visible range in the estuarine sample (PIE, Fig. 4D). In contrast, it appeared much less pronounced in the UV-B region (280–320 nm) and most acute in the UV-A region (320–400 nm) for the open-ocean sample (NPO, Fig. 4F). The coastal sample (GM, Fig. 4E) represented an intermediary between these two samples.

This pattern became even more evident when comparing the spectra of $\mathcal{M}_{q}(\lambda)$ loss averaged for three subsets corresponding to freshwaterestuarine waters ($S_{275-295} < 0.0165$, n = 8), coastal waters (0.0165 < $S_{275-295} < 0.040, n = 9$), and open-ocean waters ($S_{275-295} > 0.040, n = 9$) 10) (Fig. 5A). This comparison showed that the $\%a_{g}(\lambda)$ loss in the freshwater-estuarine samples was the highest among the three sets of samples, and was relatively homogenous throughout the visible and UV-A range (~36 %) before decreasing progressively in the UV-B range towards a minimum value (\sim 23 %) at 280 nm. In contrast, the % $a_o(\lambda)$ loss in the coastal-water samples exhibited a more pronounced spectral dependency, peaking at about 340 nm (~37 %) and decreasing progressively to <20 % at 280 nm and to <25 % at 460 nm, thereby indicating that photobleaching efficiency at wavelengths >350 nm was significantly lower in coastal waters than in more terrestrially influenced waters. The $\%a_g(\lambda)$ loss in open-ocean samples was generally lower than in the other water types and also exhibited a pronounced spectral dependency, with very low photobleaching efficiencies at 280 nm (\sim 5 %), and efficiencies peaking at about 350–360 nm (\sim 34 %) and decreasing to ~20-25 % in the visible range. However, it should be noted that the $\%a_g(\lambda)$ loss calculated for the open-ocean samples inherently carried larger uncertainties, making these measurements less reliable at wavelength >400 nm.

Differences in water temperature and exposure duration also caused significant variability in the extent of photobleaching (Fig. 5B-C). For the eight samples tested, a progressive increase in water temperature from 5 °C to 35 °C enhanced photobleaching by 50 % on average (Fig. 5B). Specifically, the average %ag(350) loss progressively increased from \sim 30 % at 5 °C, to \sim 37 % at 20 °C, and to \sim 45 % at 35 °C. A similar level of enhancement was observed throughout the spectrum from 280 to 460 nm, indicating that the effects of temperature were relatively uniform spectrally. The experiments also revealed that photobleaching became less efficient as exposure was prolonged. Specifically, the average $\%a_{\sigma}(\lambda)$ loss progressively decreased from \sim 12–25 % (depending on wavelength) on average during the first 24 h of exposure (0-24 h), to \sim 9–18 % on average during the following 24 h of exposure (24–48 h). This represented a ~25 % decrease in efficiency between time increments. This relative change with exposure duration varied with wavelength, peaking at 340 nm during the first 24 h of exposure, and increasing linearly with increasing wavelength during the following 24 h. These observations confirmed that both temperature and duration of solar exposure are also important factors regulating the efficiency of photobleaching.

3.3. Natural variability and dependencies of the measured AQY-M

Overall, the analyses based on the $\%a_g(\lambda)$ loss (Section 3.2) revealed that the composition/degradation state of CDOM (as indicated by $S_{275-295}$), the extent of solar exposure, and water temperature all had important effects on photobleaching efficiency and are likely important drivers of the observed variability in the measured AQY-M. This initial assessment was confirmed when carefully analyzing the magnitude and spectral characteristics of the *measured AQY-M* from the various samples and experiments used in this study (Fig. 6).

Most importantly, the magnitude and spectral characteristics of the *measured AQY-M* exhibited a very strong dependence on $S_{275-295}$ (Fig. 6A and Supplementary Fig. S6A). $S_{275-295}$ is a well-established

indicator of DOM origin with low (<0.015 nm⁻¹) values being indicative of fresh terrigenous DOM, and high values (>0.04 nm⁻¹) being indicative of more degraded and/or marine DOM. The overall magnitude of the measured AQY-M (average AQY-M, $\overline{\Phi}_{PB}$) showed a strong negative linear relationship ($R^2 = 0.84$ for 48-h exposures) with $S_{275-295}$ (Supplementary Fig. S6A), consistent with the decrease in $\%a_{\sigma}(\lambda)$ loss observed when transitioning from freshwater/estuarine to coastal and oceanic waters. The spectral characteristics of the *measured AQY-M* also showed a strong relationship with $S_{275-295}$ (Fig. 6A), progressing from a dominant "triangular" shape in terrestrially influenced samples $(S_{275-295} < 0.015~\text{nm}^{-1})$ to a dominant "diagonal" shape in oceanic samples ($S_{275-295} > 0.03 \text{ nm}^{-1}$). The "triangular" feature in terrestrially dominated samples indicated that UV-B photons ($\lambda_{\text{ex}} < 320 \text{ nm})$ were consistently the most efficient at decreasing CDOM absorption across the entire spectrum, and that the efficiency decreased roughly exponentially with both increasing exposure and response wavelength (i.e., towards the UV-A and visible range). In contrast, the dominant "diagonal" shape of the AQY-M in oceanic-dominated samples revealed that the maximum efficiency for a given response wavelength was at, or near, the exposure wavelength, though the efficiency also generally decreased from the UV-B to the visible. Although they were dominated by the "triangular" feature, the terrestrially influenced samples also typically featured this "diagonal feature". A decrease in overall magnitude and a progressive loss of the "triangular" feature from the rivers to the open ocean broadly summarize how the photobleaching AQY-M changes along the landocean aquatic continuum, and this change can be captured adequately by S275 205.

The effects of exposure duration on the *measured AQY-M* were more complex and varied with the composition/degradation state of CDOM (Fig. 6B and Supplementary Fig. S6B). Specifically, the effects on the magnitude and spectral characteristics of the AQY-M were subtle and variable in terrestrially influenced samples ($S_{275-295} < 0.015 \text{ nm}^{-1}$), occasionally leading to a slight increase or decrease in the overall magnitude of the AQY-M that is likely within the uncertainties of the *measured AQY-M* (Zhu et al., 2020). In contrast, the effects were more pronounced in the coastal and oceanic samples, where a prolonged duration typically led to a decrease in the overall magnitude of the AQY-M, in agreement with the increase in $\% a_g(\lambda)$ loss observed between 0–24 h and 24–48 h exposures, but without any major change in the main spectral feature. These observed uneven effects imply that the dependence of the AQY-M on exposure duration varies with CDOM origin/composition (as indicated by $S_{275-295}$).

Finally, the *measured AQY-M* exhibited a significant dependence on water temperature (Fig. 6C and Supplementary Fig. S6C). The primary effects of increasing water temperature was to increase the overall magnitude of the AQY-M, in agreement with the increase in $\%a_g(\lambda)$ loss observed from 5 to 35 °C, although some very subtle changes to the spectral characteristics between temperature treatments were also noticeable (Fig. 6C). Here, the dependency of the AQY-M magnitude followed an Arrhenius temperature dependency (Supplementary Fig. S6C), implying the effects of water temperature on the AQY-M can be adequately constrained using this type of equation.

3.4. Principal components of the AQY-M variance

The PCA of the *measured AQY-M* generated a set of principal components and their corresponding scores that can be used to approximate the observed variance in the AQY-M (Fig. 7A and Supplementary Fig. S7A). The first PC (PC1) explained 83 % of the original variance, and the PC1 eigenmatrix closely resembled the "triangular" feature typically observed in the terrestrially influenced samples. The second PC (PC2) explained 9 % of the original variance, and the PC2 eigenmatrix closely resembled the "diagonal" feature typical of the oceanic samples. The third PC (PC3) explained 4 % of the original variance and exhibited distinct spectral features. Together, the first 3 PC explained 96 % of the

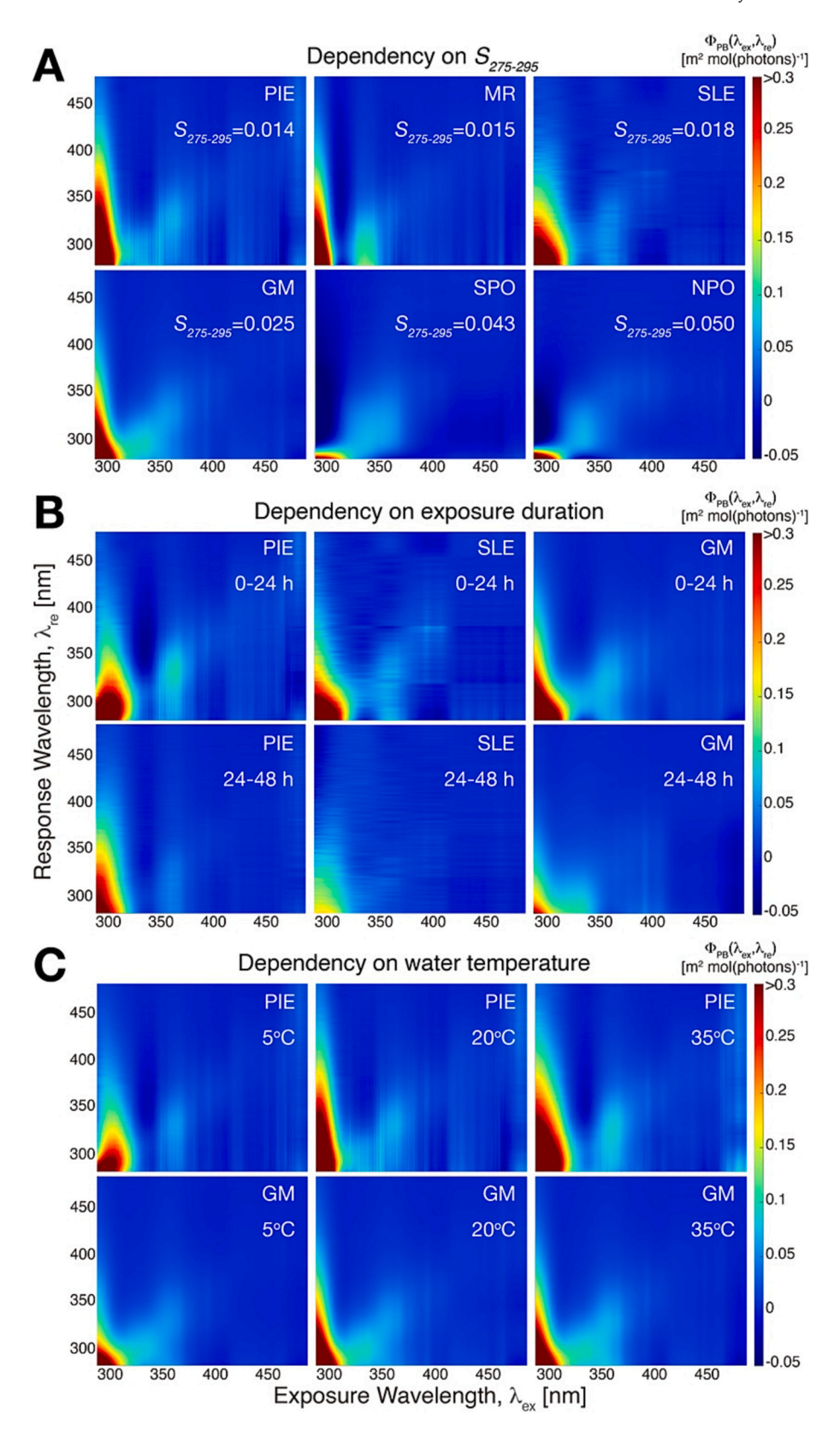


Fig. 6. Natural variability and dependencies of the measured AQY-M. (A) Variability in the measured AQY-M for water samples representing the full range of origin/degradation state, as indicated by the $S_{275-295}$ (range: $0.014-0.05~\text{nm}^{-1}$): Plum Island Estuary (PIE), Manicouagan River (MR), St-Lawrence Estuary (SLE), Gulf of Maine (GM), South Pacific Ocean (SPO), and North Pacific Ocean (NPO). All samples shown here were exposed for 48 h and at 20 °C. (B) Change in the measured AQY-M with exposure time (0–24 h versus 24–48 h) for three different water samples: Plum Island Estuary (PIE), St-Lawrence Estuary (SLE), and Gulf of Maine (GM). All samples shown here were exposed at 20 °C. (C) Variability in the measured AQY-M for two water samples exposed at different water temperatures (5, 20, and 35 °C): Plum Island Estuary (PIE) and Gulf of Maine (GM).

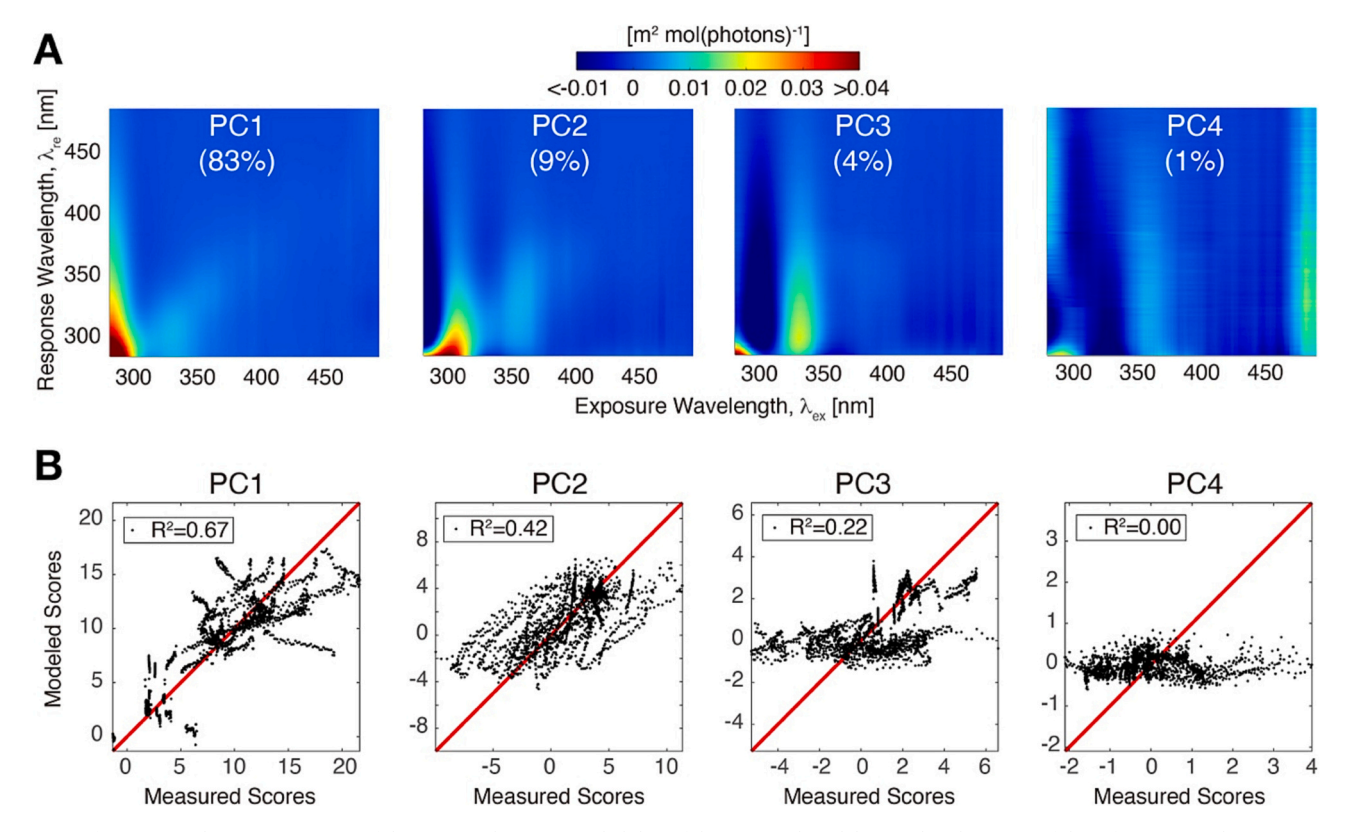


Fig. 7. First four principal components (PC) of the measured AQY-M, and ability of the proposed model to predict the scores of these four principal components. (A) First four PC of the measured AQY-M database determined by a principal component analysis. The fractions (%) of the initial variance explained by the first, second, third, and fourth PC are overlaid on each PC matrix (83 %, 9 %, 4 %, and 1 %, respectively). (B) Measured versus modeled scores for the first four PC. The red line represents the 1-to-1 line and the R^2 is coefficient of determination of a linear fit of the modeled scores on the measured scores. The modeled scores were estimated from three predictor variables (water temperature, $S_{275-295}$, and the standardized solar exposure t_{std}).

observed variance and can therefore reproduce the *measured AQY-M* with good accuracy if the scores are known. The fourth PC accounted for only 1 % of the original variance and exhibited seemingly more random features in the 2-dimensional spectral domain of the AQY-M. This fourth component, as well as the subsequent ones, are likely representing noise that do not carry useful information to reproduce the AQY-M.

3.5. Predicting the AQY-M in estuarine, coastal, and oceanic waters

The predictive model developed in this study (see Section 2.7) enabled reasonable predictions of scores for the first three PCs (Fig. 7B and Supplementary Fig. S7B). This simple model using three simple predictive variables ($S_{275-295}$, T, t_{std}) was able to capture 67 %, 42 %, and 22 % of the variability of PC1, PC2, PC3 scores, respectively, as indicated by a completely independent validation strategy (i.e., leave-1 experiment-out validation). The model captured 70 %, 48 % and 31 % of the variability respectively when the data from all 43 experiments were used for both training and validation (Supplementary Fig. S8). The model had no capability to predict the scores of PC4, thereby further negating the need to include a fourth PC in the model. Approaches applying empirical models including a multiple-linear-regression (MLR) model and various machine-learning approaches did not perform as well (based on the independent validations) as the proposed model (Section 2.7; Supplementary Text S6, Figs. S9-S10, Tables S6-S7). Among the different machine-learning methods used here, the Support Vector Machine (SVM) performed best, but all fell short of the proposed model's performance (Supplementary Fig. S10 and Table S8) and therefore were not considered further in the rest of this study.

The use of $t_{\rm std}$ as a predictor variable in the model—in addition to $S_{275-295}$ and T—was critical for predicting the scores of PC2 accurately. The relationship between $S_{275-295}$ and PC scores, which is central to the

AQY-M predictive model, changed with increasing solar exposure duration (Supplementary Fig. S11). The dependence of the relationship between $S_{275-295}$ and PC scores on $t_{\rm std}$ was relatively weak for PC1 and PC3. However, it was highly significant for the scores of PC2. Specifically, while a lack of relationship between $S_{275-295}$ and the PC2 scores was observed when $t_{\rm std}$ was close to 0, the relationship became increasingly significant as $t_{\rm std}$ became longer. As a result of this dependency, the ability to predict the PC scores decreased significantly when $t_{\rm std}$ was omitted from the model's formulation (Supplementary Fig. S12). In particular, the scores of PC2 were poorly predicted (R² decreased from 0.42 to 0.11) when using $S_{275-295}$ and T as sole predictors. These observations confirmed the importance of incorporating $t_{\rm std}$ as a predictive variable when modeling the AQY-M.

The ability of the proposed model to reproduce the measured AQY-M from the three simple predictive variables ($S_{275-295}$, T, t_{std}) was further assessed, qualitatively, by directly comparing the measured and modeled AQY-M (Fig. 8A). The comparison revealed the model was able to reproduce the overall magnitude and major spectral features of the measured AQY-M reasonably well across the full range of representative water types considered in this study (as indicated by $S_{275-295}$ range of 0.014 to 0.05 nm⁻¹). Although minor differences between measured and modeled AQY-M were still evident, the model adequately reproduced the "triangular" feature in the terrestrially influenced samples and the "diagonal" feature in the oceanic samples. The good performance of the proposed model was further confirmed when comparing the measured and modeled $a_g(\lambda)$ spectra after 48 h of exposure relative to those measured at t_0 (Fig. 8B). Specifically, the comparison showed that the modeled $a_{\varrho}(\lambda)$ spectra (derived by using the modeled AQY-M) closely approximated the measured $a_g(\lambda)$ spectra, reproducing accurately the magnitude and spectral shape of the photobleached $a_{\varrho}(\lambda)$ in both the terrestrially influenced and oceanic samples.

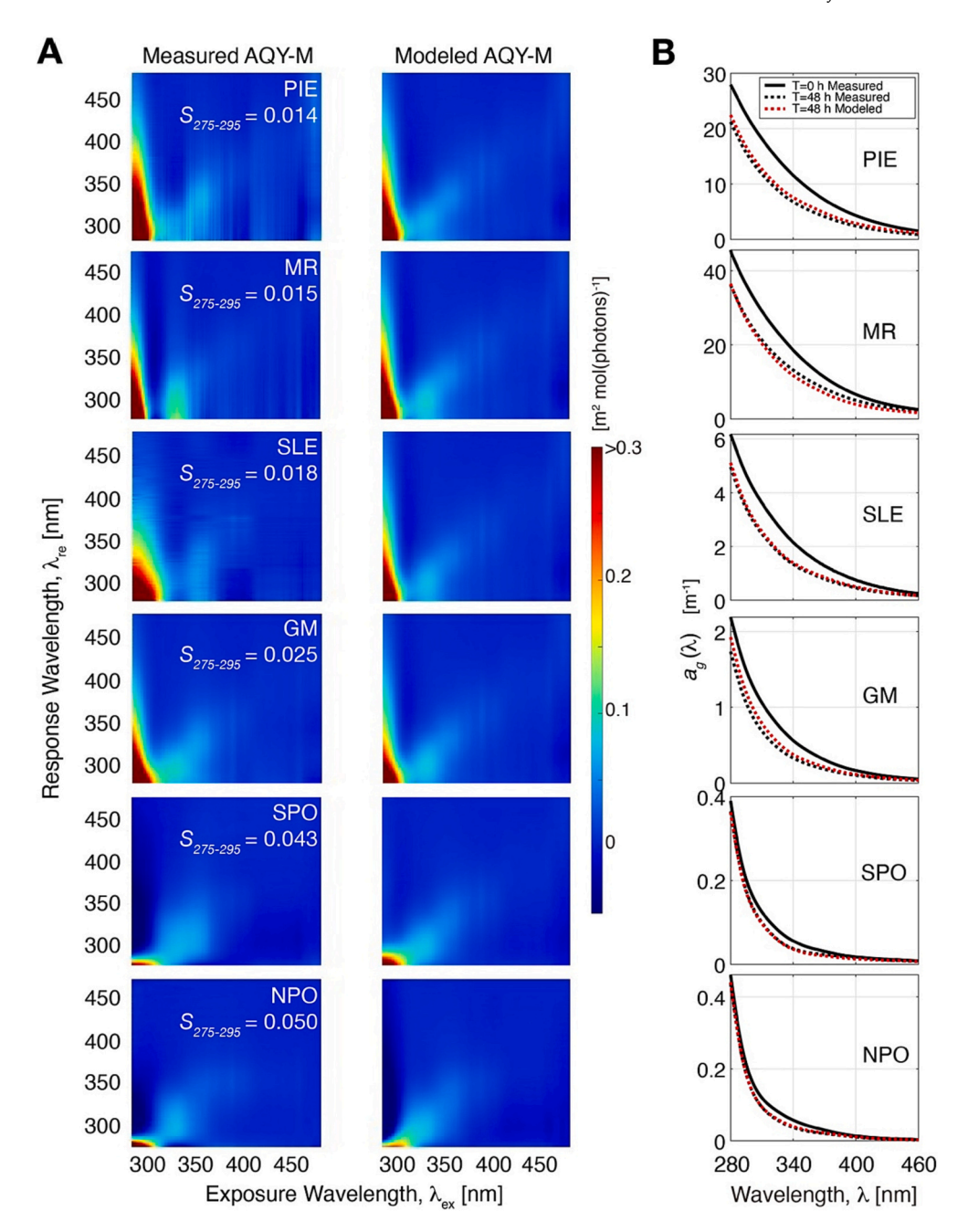


Fig. 8. Demonstration of the proposed model's ability to reproduce the measured AQY-M and the corresponding change in $a_g(\lambda)$ caused by photobleaching for six contrasting water samples. (A) Comparison of measured and modeled AQY-M shown here for six contrasting water samples collected along the land-ocean aquatic continuum: Plum Island Estuary (PIE), Manicouagan River (MR), St-Lawrence Estuary (SLE), Gulf of Maine (GM), South Pacific Ocean (SPO), and North Pacific Ocean (NPO). (B) Comparison of measured and modeled $a_g(\lambda)$ spectra after 48 h of solar exposure, relative to the measured $a_g(\lambda)$ at initial time $t_0=0$ h (prior to solar exposure). The modeled $a_g(\lambda)$ spectra in panels (A) and (B) were derived from the leave-1 experiment-out cross-validation, and therefore show independent retrievals.

A quantitative assessment of the model's ability to reproduce the $a_g(\lambda)$ measured after 24 and 48 h of exposure confirmed the viability of the model (Fig. 9). The two entirely independent validation strategies (i. e., the leave-1 experiment-out, and the extra independent validation) showed that the model can reproduce the measured $a_g(\lambda)$ observed at t_{24} and t_{48} with very reasonable uncertainties across the entire range of values and across the UV-blue region (Fig. 9A). Specifically, the leave-1 experiment-out validation showed that the vast majority of the modeled values were within ± 8 , 15, 20, and 30 % of measured values at 280, 340, 400 and 460 nm respectively, with corresponding median errors of about ± 3 , 6, 10, and 15 % (Fig. 9B). The extra validation, which uses an entirely independent data set corresponding to an environment not represented in the training data set, showed even better performance

with the majority of modeled values within ± 6 , 8, 10, and 15 % of measured values at 280, 340, 400 and 460 nm respectively, and corresponding median errors of about ± 4 , 3, 5, and 8 % (Fig. 9B). The model also performed well when predicting $S_{275-295}$ measured at t_{24} and t_{48} , with relative uncertainties typically within ± 1 to 5 % across the range of $\sim 0.015-0.07$ nm⁻¹ (Supplementary Fig. S13). The model performed reasonably well when predicting $S_{350-400}$ but less well than at $S_{275-295}$ (± 1 to 10 %), though the range was smaller ($\sim 0.015-0.025$ nm⁻¹). A direct comparison of the modeled change in $a_g(\lambda)$ during exposure, $\Delta a_g(\lambda)$, also confirmed the good performance of the model, though uncertainties in the modeled $\Delta a_g(\lambda)$ are larger (Supplementary Fig. S14).

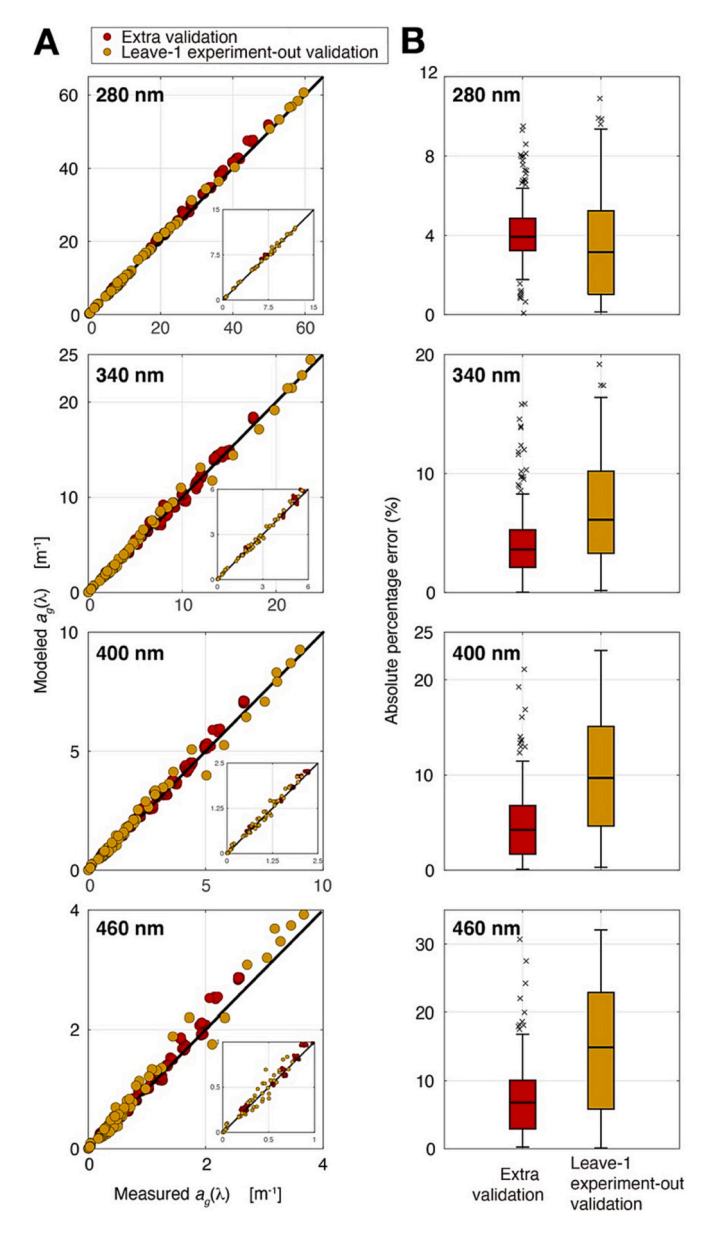


Fig. 9. Validation of the model's ability to reproduce the CDOM absorption coefficient measured after 24 or 48 h of exposure. (A) Modeled versus measured $a_g(\lambda)$ after 24 and 48 h of exposure shown here at 280, 340, 400, and 460 nm. Validation results are from the leave-1 experiment-out cross-validations (gold color) and from the independent extra validation (red color). The black line represents the 1-to-1 line and the inset in each panel is a close-up view of the comparison at low values (approximately the first 25 % of the full range of values). (B) Corresponding estimates of absolute percent error in the modeled $a_g(\lambda)$ relative to the measured $a_g(\lambda)$ shown here at 280, 340, 400, and 460 nm.

4. Discussion

4.1. Variability of the photobleaching AQY-M along the land-ocean aquatic continuum

This study revealed that the magnitude and spectral characteristics of the CDOM photobleaching AQY-M vary substantially across the land-ocean aquatic continuum. Specifically, the AQY-M of terrigenous CDOM has a higher overall magnitude than that of oceanic CDOM and is dominated by a "triangular" spectral feature indicating that: 1) UV-B radiation is most efficient at degrading CDOM absorption, 2) the efficiency decreases exponentially with increasing exposure wavelength, and 3) the loss of absorption extends over the entire spectrum. During

solar exposure in natural waters, this specific AQY-M therefore leads to significant loss of CDOM absorption across the entire UV-visible spectrum. This "photobleaching behavior" of terrigenous CDOM is consistent with the photochemical degradation of intramolecular charge-transfer interactions, which are chemical moieties of terrestrial origin thought to be largely responsible for CDOM absorption in the visible range (Boyle et al., 2009; Del Vecchio and Blough, 2004; Sharpless and Blough, 2014). The dominant "triangular" pattern of terrigenous CDOM progressively disappears towards the open ocean, where a remnant "diagonal" pattern (which was also observed in terrigenous CDOM) becomes increasingly dominant. This is consistent with the diagonal spectral photobleaching pattern observed by Tzortziou et al. (2007) in coastal samples. This gradual loss of the "triangular" pattern across the landocean continuum is consistent with the efficient photochemical degradation of intramolecular charge-transfer interactions as solar exposure of terrigenous CDOM becomes prolonged during transport in sunlit waters. In contrast, the remnant "diagonal" pattern indicates that photobleaching efficiency in the ocean is highest at or near the exposure wavelength, which is consistent with the degradation of independent chromophores rather than that of intramolecular charge-transfer interactions. This transition from "triangular" to "diagonal" pattern thus suggests that independent chromophores are preferentially preserved and dominate CDOM absorption in the open ocean. Although this evidently warrants more targeted investigations, these observations are generally consistent with the two main conceptual models of CDOM absorption (intramolecular charge-transfer interactions versus superposition of independent chromophores) currently put forward (McKay, 2020).

These important differences in AQY-M indicate that solar exposure alters the CDOM absorption coefficient spectrum in variable ways across the land-ocean continuum. Specifically, solar exposure of terrigenous CDOM leads to a substantial loss in CDOM absorption across the UV-visible spectrum that is highest and spectrally uniform in the visible and decreases moderately towards the UV-B range. This effect is consistent with an increase in the spectral slope coefficient of CDOM absorption typically observed during photobleaching and along the salinity gradient (Del Vecchio and Blough, 2002; Fichot and Benner, 2012; Vodacek et al., 1997). In sharp contrast, solar exposure of openocean CDOM consistently leads to significant but spectrally distinct changes in CDOM absorption that peak strongly in the UV-A range (~350–360 nm) and is lower in the visible range and minimal in the UV-B region. This spectral imbalance has a major impact on the spectral shape of open-ocean CDOM, consistent with previous observations of the effects of photobleaching on open-ocean CDOM (Swan et al., 2012; Yamashita et al., 2013). This effect of photobleaching is also consistent with the spectral shape of CDOM observed in the surface open ocean, which typically exhibits a characteristic break around 350 nm (Nelson and Siegel, 2013; Stedmon and Nelson, 2015; Yamashita et al., 2013). The effects of solar exposure on coastal CDOM represented an intermediary between these two extreme cases.

The AQY-M is also significantly influenced by water temperature and the extent/duration of solar exposure. These observations are ubiquitous for all samples and confirmed previous observations made for a single river-water sample (Zhu et al., 2020). Water temperature mostly affected the overall magnitude of the AQY-M, with little influence on the spectral characteristics, consistent with an earlier report that increasing water temperature enhances photobleaching (Song et al., 2017). This dependence on temperature and its reasonable description using an Arrhenius equation suggest that photobleaching is, at least partially, driven by secondary reactions involving the photochemical production of intermediary radicals (Mopper et al., 2015). The dependence of the AQY-M on the extent/duration of solar exposure is more spectrally complex, although it generally leads to a decrease in photobleaching efficiency and a preferential loss of the triangular pattern as exposure is prolonged. These observations are also consistent with the idea that photobleaching progressively degrades complexes involved

intramolecular charge-transfer interactions as terrigenous CDOM transits through the sunlit waters of the land-ocean continuum, thereby changing the structure, composition of CDOM, and exposing new moieties to photodegradation.

Salinity (ionic strength) and pH are water properties known to have an influence on photobleaching (Song et al., 2017), and are therefore a likely source of AQY-M variability. Although the distinct effects of ionic strength and pH on the AQY-M were not explicitly tested in this study, their influences are inherently considered through the diversity of water samples used here. Furthermore, the large gradient in salinity from freshwater to the open ocean is mimicked reasonably well by the change in $S_{275-295}$, which is the main predictor driving the AQY-M model. Variations in pH is a source of unconstrained variability, though it should be noted that the pH only varies over a relatively narrow range in most water types considered in this work.

4.2. Predictability of the AQY-M and applicability of the model

This new understanding of the AQY-M variability and of its driving factors informed the development of a simple model capable of reproducing the AQY-M in most surface waters. Knowledge of the $S_{275-295}$, water temperature, and standardized solar exposure were sufficient to reproduce the AQY-M of a wide range of samples with accuracy. In particular, the model was able to reproduce the magnitude and primary spectral features of the contrasting AQY-M encountered along the landocean continuum. The modeled AQY-M then facilitated the calculation of accurate and spectrally realistic changes in CDOM absorption coefficient spectra caused by photobleaching. We expect the model to be applicable to most surface waters ranging from rivers and coastal wetlands to the open ocean. However, the applicability of the model beyond surface waters (e.g., mesopelagic and deep ocean) and to atypical sources of CDOM (e.g., groundwater, sediment porewater, plant leachate, etc....) remains unknown and would require further investigation.

A major strength of the proposed model is the possibility of implementation on regional and global scales using remotely sensed estimates of the model predictors. First, the spectral slope coefficient, $S_{275-295}$, has been shown to be retrievable empirically from ocean color remote sensing (Cao et al., 2018; Fichot et al., 2013, 2014). Second, sea-surface temperature is a standard widely available remote sensing product on large and global scales (Merchant et al., 2019). Third, photochemical models informed by remote sensing and modeled mixed layer depth can provide estimates of solar exposure from which t_{std} can be derived (Fichot and Miller, 2010; Schmidtko et al., 2013; Zhu and Kieber, 2020). The retrieval of these three parameters using remote sensing can facilitate the calculation of spatially explicit distributions of AQY-M in the surface ocean that can be used for a global assessment of photobleaching rates.

5. Concluding remark

This work applied a recently developed experimental method (Zhu et al., 2020) on a wide range of contrasting samples to provide a new understanding of the natural variability of the CDOM photobleaching AQY-M. It also facilitated the development of a new model capable of predicting this variability along the aquatic land-ocean continuum. The next step in this work will be the implementation of this model into a remote-sensing informed, process-based photochemical model (Fichot and Miller, 2010) to calculate photobleaching rates on large scales and shed new light on the significance of photobleaching as a sink of CDOM along the aquatic land-ocean continuum.

Credit authorship contribution statement

XZ and CGF conceived and directed the study, and designed the experiments and the overall methodology. XZ conducted all experiments

to measure AQY-M, analyzed the data, and developed the model. MWW and JH conducted the photochemical experiments of the extra validation. XZ and CGF wrote the manuscript and made the figures. All authors contributed to the collection of samples and field data. All authors commented on the manuscript.

Declaration of competing interest

The authors declare that they have no known competing financial interests or personal relationships that could have appeared to influence the work reported in this paper.

Data availability

The model coefficients and MatLAB scripts to implement the model are available on Zenodo (doi: 10.5281/zenodo.10207263). These files can also be made available upon request.

Acknowledgements

This work was directly and primarily funded by a NASA Remote Sensing of Water Quality grant (80NSSC18K0344) to CGF. The sample collection was also partly supported by the Future Investigators in NASA Earth and Space Science and Technology grant (80NSSC20K1648), the NASA Earth Venture Suborbital-3 Program (NNH17ZDA001N-EVS3) for the Delta-X mission, the National Science Foundation-supported Plum Island Ecosystems Long-Term Ecological Research Program (OCE-2224608), and the WISE-Man Project funded by the Canadian Space Agency (18FARIMA20). The authors also acknowledge the Boston University Warren-McLeod Graduate Fellowship in Marine Science and the China Scholarship Council for graduate support of XZ. The authors thank the crew of the R/V Ronald H. Brown and the chief scientists (Rolf Sonnerup, Brendan Carter, and Denis Volkov) onboard the GO-SHIP cruises P18 (33RO20161119) and IO7N (33RO20180423), who facilitated the collection of the open-ocean samples used in this study. They also thank the crew of the R/V Meteor and chief scientist Matthias Zabel onboard cruise M157 in 2019 who facilitated the collection of coastalupwelling samples used in this study.

Appendix A. Supplementary data

Supplementary data to this article can be found online at $\frac{\text{https:}}{\text{doi.}}$ org/10.1016/j.scitotenv.2023.168670.

References

- Bonelli, A.G., Loisel, H., Jorge, D.S.F., Mangin, A., d'Andon, O.F., Vantrepotte, V., 2022. A new method to estimate the dissolved organic carbon concentration from remote sensing in the global open ocean. Remote Sens. Environ. 281 https://doi.org/10.1016/J.RSE.2022.113227.
- Boyle, E.S., Guerriero, N., Thiallet, A., Del Vecchio, R., Blough, N.V., 2009. Optical properties of humic substances and CDOM: Relation to structure. Environ. Sci. Technol. 43, 2262–2268. https://doi.org/10.1021/ES803264G.
- Cao, F., Tzortziou, M., Hu, C., Mannino, A., Fichot, C.G., Del Vecchio, R., Najjar, R.G., Novak, M., 2018. Remote sensing retrievals of colored dissolved organic matter and dissolved organic carbon dynamics in North American estuaries and their margins. Remote Sens. Environ. 205, 151–165. https://doi.org/10.1016/J.RSE.2017.11.014.
- Del Vecchio, R., Blough, N.V., 2002. Photobleaching of chromophoric dissolved organic matter in natural waters: Kinetics and modeling. Mar. Chem. 78, 231–253. https:// doi.org/10.1016/S0304-4203(02)00036-1.
- Del Vecchio, R., Blough, N.V., 2004. On the origin of the optical properties of humic substances. Environ. Sci. Technol. 38, 3885–3891. https://doi.org/10.1021/ ESCARCES.
- Druffel, E.R.M., Griffin, S., Lewis, C.B., Rudresh, M., Garcia, N.G., Key, R.M., McNichol, A.P., Hauksson, N.E., Walker, B.D., 2021. Dissolved organic radiocarbon in the Eastern Pacific and Southern Oceans. Geophys. Res. Lett. 48, e2021GL092904 https://doi.org/10.1029/2021GL092904.
- Fichot, C.G., Benner, R., 2011. A novel method to estimate DOC concentrations from CDOM absorption coefficients in coastal waters. Geophys. Res. Lett. 38 https://doi. org/10.1029/2010GL046152.
- Fichot, C.G., Benner, R., 2012. The spectral slope coefficient of chromophoric dissolved organic matter (\$ 275–295) as a tracer of terrigenous dissolved organic carbon in

- river-influenced ocean margins. Limnol. Oceanogr. 57, 1453–1466. https://doi.org/ 10.4319/L0.2012.57.5.1453.
- Fichot, C.G., Benner, R., 2014. The fate of terrigenous dissolved organic carbon in a river-influenced ocean margin. Glob. Biogeochem. Cycles 28, 300–318. https://doi.org/10.1002/2013GB004670.
- Fichot, C.G., Miller, W.L., 2010. An approach to quantify depth-resolved marine photochemical fluxes using remote sensing: application to carbon monoxide (CO) photoproduction. Remote Sens. Environ. 114, 1363–1377. https://doi.org/10.1016/ J.RSE.2010.01.019.
- Fichot, C.G., Kaiser, K., Hooker, S.B., Amon, R.M.W., Babin, M., Bélanger, S., Walker, S. A., Benner, R., 2013. Pan-Arctic distributions of continental runoff in the Arctic Ocean. Sci. Rep. 3 https://doi.org/10.1038/SREP01053.
- Fichot, C.G., Lohrenz, S.E., Benner, R., 2014. Pulsed, cross-shelf export of terrigenous dissolved organic carbon to the Gulf of Mexico. J. Geophys. Res. Oceans 119, 1176–1194. https://doi.org/10.1002/2013JC009424.
- Fichot, C.G., Tzortziou, M., Mannino, A., 2023. Remote sensing of dissolved organic carbon (DOC) stocks, fluxes and transformations along the land-ocean aquatic continuum: advances, challenges, and opportunities. Earth Sci. Rev. 242, 104446 https://doi.org/10.1016/J.EARSCIREV.2023.104446.
- Goldstone, J.V., Del Vecchio, R., Blough, N.V., Voelker, B.M., 2004. A multicomponent model of chromophoric dissolved organic matter photobleaching. Photochem. Photobiol. 80, 52. https://doi.org/10.1562/TM-03-17.1.
- Hansen, A.M., Kraus, T.E.C., Pellerin, B.A., Fleck, J.A., Downing, B.D., Bergamaschi, B.A., 2016. Optical properties of dissolved organic matter (DOM): effects of biological and photolytic degradation. Limnol. Oceanogr. 61, 1015–1032. https://doi.org/10.1002/LNO.10270
- Helms, J.R., Stubbins, A., Perdue, E.M., Green, N.W., Chen, H., Mopper, K., 2013. Photochemical bleaching of oceanic dissolved organic matter and its effect on absorption spectral slope and fluorescence. Mar. Chem. 155, 81–91. https://doi.org/ 10.1016/J.MARCHEM.2013.05.015.
- Hickman, A.E., Dutkiewicz, S., Williams, R.G., Follows, M.J., 2010. Modelling the effects of chromatic adaptation on phytoplankton community structure in the oligotrophic ocean. Mar. Ecol. Prog. Ser. 406, 1–17. https://doi.org/10.3354/MEPS08588.
- Hill, V.J., 2008. Impacts of chromophoric dissolved organic material on surface ocean heating in the Chukchi Sea. J. Geophys. Res. Oceans 113. https://doi.org/10.1029/ 2007JC004119.
- Kouassi, A.M., Zika, R.G., 1992. Light-induced destruction of the absorbance property of dissolved organic matter in seawater. Toxicol. Environ. Chem. 35, 195–211. https:// doi.org/10.1080/02772249209357816.
- Mannino, A., Novak, M.G., Nelson, N.B., Belz, M., Berthon, J.-F., Blough, N.V., Boss, E., Bricaud, A., Chaves, J., Del Castillo, C., Del Vecchio, R., D'Sa, E.J., Freeman, S., Matsuoka, A., Miller, R.L., Neeley, A., Röttgers, R., Tzortziou, M., Werdell, 2019. Measurement protocol of absorption by chromophoric dissolved organic matter (CDOM) and other dissolved materials. In: Mannino, A., Novak, M.G. (Eds.), Inherent Optical Property Measurements and Protocols: Absorption Coefficient, IOCCG Ocean Optics and Biogeochemistry Protocols for Satellite Ocean Colour Sensor Validation. IOCCG. Dartmouth, NS. Canada.
- McKay, G., 2020. Emerging investigator series: critical review of photophysical models for the optical and photochemical properties of dissolved organic matter. Environ Sci Process Impacts 22, 1139–1165. https://doi.org/10.1039/D0EM00056F.
- Mena, C., Reglero, P., Hidalgo, M., Sintes, E., Santiago, R., Martín, M., Moyà, G., Balbín, R., 2019. Phytoplankton community structure is driven by stratification in the oligotrophic mediterranean sea. Front. Microbiol. 10, 1698. https://doi.org/ 10.3389/FMICB.2019.01698/BIBTEX.
- Merchant, C.J., Embury, O., Bulgin, C.E., Block, T., Corlett, G.K., Fiedler, E., Good, S.A., Mittaz, J., Rayner, N.A., Berry, D., Eastwood, S., Taylor, M., Tsushima, Y., Waterfall, A., Wilson, R., Donlon, C., 2019. Satellite-based time-series of sea-surface

- temperature since 1981 for climate applications. Sci. Data 6 (1), 1–18. https://doi.org/10.1038/s41597-019-0236-x.
- Mopper, K., Kieber, D.J., Stubbins, A., 2015. Marine photochemistry of organic matter: processes and impacts. In: Biogeochemistry of Marine Dissolved Organic Matter: Second Edition, pp. 389–450. https://doi.org/10.1016/B978-0-12-405940-5.00008-
- Murphy, K.R., Timko, S.A., Gonsior, M., Powers, L.C., Wünsch, U.J., Stedmon, C.A., 2018. Photochemistry illuminates ubiquitous organic matter fluorescence spectra. Environ. Sci. Technol. 52, 11243–11250. https://doi.org/10.1021/ACS. EST 8802648
- Nelson, N.B., Siegel, D.A., 2013. The global distribution and dynamics of chromophoric dissolved organic matter. Annu. Rev. Mar. Sci. 5, 447–476. https://doi.org/10.1146/ ANNUREV-MARINE-120710-100751.
- Osburn, C.L., Zagarese, H.E., Morris, D.P., Hargreaves, B.R., Cravero, W.E., 2001. Calculation of spectral weighting functions for the solar photobleaching of chromophoric dissolved organic matter in temperate lakes. Limnol. Oceanogr. 46, 1455–1467. https://doi.org/10.4319/LO.2001.46.6.1455.
- Pegau, W.S., Gray, D., Zaneveld, J.R.V., 1997. Absorption and attenuation of visible and near-infrared light in water: dependence on temperature and salinity. Appl. Opt. 36, 6035. https://doi.org/10.1364/AO.36.006035.
- Schmidtko, S., Johnson, G.C., Lyman, J.M., 2013. MIMOC: a global monthly isopycnal upper-ocean climatology with mixed layers. J. Geophys. Res. Oceans 118, 1658–1672. https://doi.org/10.1002/JGRC.20122.
- Sharpless, C.M., Blough, N.V., 2014. The importance of charge-transfer interactions in determining chromophoric dissolved organic matter (CDOM) optical and photochemical properties. Environ Sci Process Impacts 16, 654–671. https://doi. org/10.1039/C3EM00573A.
- Song, G., Li, Y., Hu, S., Li, G., Zhao, R., Sun, X., Xie, H., 2017. Photobleaching of chromophoric dissolved organic matter (CDOM) in the Yangtze River estuary kinetics and effects of temperature, pH, and salinity. Environ Sci Process Impacts 19, 861–873. https://doi.org/10.1039/C6EM00682E.
- Stedmon, C.A., Nelson, N.B., 2015. The optical properties of DOM in the ocean. In: Biogeochemistry of Marine Dissolved Organic Matter: Second Edition, pp. 481–508. https://doi.org/10.1016/B978-0-12-405940-5.00010-8.
- Swan, C.M., Nelson, N.B., Siegel, D.A., Kostadinov, T.S., 2012. The effect of surface irradiance on the absorption spectrum of chromophoric dissolved organic matter in the global ocean. Deep Sea Res. 1 Oceanogr. Res. Pap. 63, 52–64. https://doi.org/ 10.1016/J.DSR.2012.01.008.
- Tzortziou, M., Osburn, C.L., Neale, P.J., 2007. Photobleaching of dissolved organic material from a tidal marsh-estuarine system of the Chesapeake Bay. Photochem. Photobiol. 83, 782–792. https://doi.org/10.1111/J.1751-1097.2007.00142.X.
- Vodacek, A., Blough, N.V., DeGrandpre, M.D., Peltzer, E.T., Nelson, R.K., 1997. Seasonal variation of CDOM and DOC in the Middle Atlantic Bight: terrestrial inputs and photooxidation. Limnol. Oceanogr. 42, 674–686. https://doi.org/10.4319/ LO.1997.42.4.0674.
- Yamashita, Y., Nosaka, Y., Suzuki, K., Ogawa, H., Takahashi, K., Saito, H., 2013. Photobleaching as a factor controlling spectral characteristics of chromophoric dissolved organic matter in open ocean. Biogeosciences 10, 7207–7217. https://doi. org/10.5194/BG-10-7207-2013.
- Zhu, Y., Kieber, D.J., 2020. Global model for depth-dependent carbonyl photochemical production rates in seawater. Glob. Biogeochem. Cycles 34, e2019GB006431. https://doi.org/10.1029/2019GB006431.
- Zhu, X., Miller, W.L., Fichot, C.G., 2020. Simple method to determine the apparent quantum yield matrix of CDOM photobleaching in natural waters. Environ. Sci. Technol. 54, 14096–14106. https://doi.org/10.1021/ACS.EST.0C03605/ASSET/ IMAGES/MEDIUM/ES0C03605_M021.GIF.